FINAL SCIENTIFC AND TECHNICAL REPORT

Report Title:

Computational Design and Experimental Validation of New Thermal Barrier Systems

Type of Report: Final Scientific and Technical

Reporting Period Start Date: 10/1/2010

Reporting Period End Date: 3/30/2015

Principal Author(s): Shengmin Guo

Date Report was Issued: June 2015

DOE Award Number: DE-FE0004734

Name and Address of Submitting Organization:

Louisiana State University and A & M College
Baton Rouge, LA, 70803-2701

ABSTRACT

The focus of this project is on the development of a reliable and efficient *ab initio* based computational high temperature material design method which can be used to assist the Thermal Barrier Coating (TBC) bond-coat and top-coat design. Experimental evaluations on the new TBCs are conducted to confirm the new TBCs' properties. Southern University is the subcontractor on this project with a focus on the computational simulation method development.

We have performed *ab initio* density functional theory (DFT) method and molecular dynamics simulation on screening the top coats and bond coats for gas turbine thermal barrier coating design and validation applications. For experimental validations, our focus is on the hot corrosion performance of different TBC systems. For example, for one of the top coatings studied, we examined the thermal stability of $TaZr_{2.75}O_8$ and confirmed it's hot corrosion performance.

TABLE OF CONTENTS

EXECUTIVE SUMMARY

In the theoretical/simulation part, the interatomic potentials for pure metals, binary alloys or systems were calculated using a recently developed repulsive kinetic energy fitting scheme to reduce the computation expense on performing molecular dynamics (MD) simulations. For ternary and systems containing *f*-electron elements, such as Ta and Ir, we used traditional *ab initio* DFT model with relative small cell sizes. Here, the evolutionary algorithm was also applied to obtain the most stable structures and accelerate the structure optimization. The integrated materials design package MedeA, combined the database searching, model building, simulation job submission, data processing, visualization, and analysis etc., was used to assist our thermal barrier coatings design and student training. For the model systems, we simulated the Y and Ta doping effect in bond coat and Ta_2O_5 dopant effect in top coat ZrO_2. The results were summarized and used to guide experiment validations. Our simulation works were performed on Louisiana Optical Network Initiative (LONI) and LSU super computers and dislocation dynamics texture experiment was conducted at LBNL beamline 12-2-2.

In the experimental validation part, our focus was on alternative coating materials other than the well-established yttria stabilized zirconia (YSZ) system. The study consisted two main approaches: 1. alternative materials to ZrO_2-based systems (rare earth zirconate), and 2. alternative stabilizers to Y_2O_3 for ZrO_2-based systems(CeO2,Ta_2O_5,TiO_2). For the first approach, we studied gadolinium zirconate ($Gd_2Zr_2O_7$), and for the second approach, our focus was on zirconium tantalum oxides with single orthorhombic phase ($TaZr_{2.75}O_8$). Because YSZ is susceptible to hot corrosion, one of our main experimental evaluations is to examine the hot corrosion performance of both gadolinium zirconate ($Gd_2Zr_2O_7$) and ZrO_2/Ta_2O_5 compounds. Different compositions of ZrO_2-Ta_2O_5 samples and gadolinium zirconate samples in the presence of molten mixture of Na_2SO_4 + V_2O_5 at elevated temperatures were tested. For the ZrO_2-Ta_2O_5 samples, the compositions were selected to form tetragonal and orthorhombic phases of zirconium-tantalum oxides. Results showed that orthorhombic zirconium-tantalum oxide was more stable, both thermally and chemically in Na_2SO_4+V_2O_5 media at 1100˚C, and showed a better hot corrosion resistance than the tetragonal phase.

Students and postdocs were trained to setup the needed *ab initio* DFT MD simulation models, perform high performance computing (HPC) simulations, process and analyze the simulation data sets, write analysis reports, and present the results and conclusions through participating group meeting, workshop, international conferences etc. They were also trained in sample preparation—including the preparation of TBC samples using plasma spray system, XRD, TGA, DSC, and synchrotron XRD materials characterization techniques such as the full width at half maximum (FWHM) synchrotron XRD data processing, radial texture measurement, and data interpretation. Partly supported by this project, ten peer reviewed papers were published.

REPORT DETAILS

1. Simulation Methods:

In this project, the Materials Design software (MedeA) package is used for all the models setup and part of the data processing and visualization, e.g. the interface models setup and phonon related Gibbs free energy calculation were both carried out using this package. All of our MD simulation is based on the DFT method. All the HPC MD simulation works were performed on Louisiana Optical Network Initiative (LONI) and LSU supercomputers.

The efficient DFT based *ab initio* MD simulation and property calculation was used in computational work of the TBC substrate simulation. The formalism to obtain the inter-atomic potentials in this part is based on the calculations of the electron densities and the total energies $E_{total}(\rho)$ of the many-body system:

$$\mathrm{E_{total}}(\rho) = \mathrm{T} + \sum_{lm} \int \rho(\vec{r})dv \frac{-e^2 Z_m}{\left|\vec{r} - \vec{\tau}_m - \vec{R}_l\right|} + \frac{1}{2}\int \frac{\rho(\vec{r})\rho(\vec{r}\,')}{\left|\vec{r} - \vec{r}\,'\right|} dvdv' + \mathrm{E_{xc}}(\rho) + \frac{1}{2}\sum_{mn} \frac{e^2 Z_m Z_n}{\left|\vec{\tau}_m - \vec{\tau}_n\right|}, \quad (1.1)$$

where T is the total kinetic energy of the many-electron system; ρ is the electron density in real space; $\vec{\tau}_m$ and Z_m are the position and the nuclear charge of the m-th ion; $\vec{R}_l$ is the translational vector; and $E_{xc}(\rho)$ is the exchange-correlation energy of the many-electron system. The kinetic energy part, which is hard to compute, is expressed as a universal binding energy relation, in which the repulsive-core energy is determined by fitting the accurate *ab initio* DFT total energy results, i.e. a functional of total energy based on charge density. Thus the method is still *ab initio*. On the other hand, our method takes advantage of efficient classical MD method to gain the accurate and fast material design from the *ab initio* MD simulation. So far pure metals and many binary systems were tested and compared the prediction results with corresponding experiment ones and they are all in consistent to each other. For ternary and more element systems and the ones include *f* electrons, we used the traditional DFT MD method with related smaller cell sizes to perform simulations. In structure screening, we used recently developed evolutional algorithm to accelerate the structure optimization. The Figure 1.1 shows a typical model used in simulation for $Ta_{20}Nb_{20}Hf_{20}Zr_{20}Ti_{20}$.

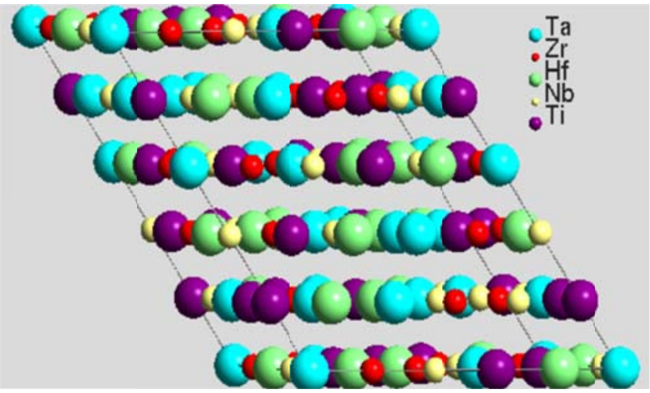

Fig 1.1 The unit cell model used in simulation for $Ta_{20}Nb_{20}Hf_{20}Zr_{20}Ti_{20}$.

2. Experimental Methods:

The current material of choice for gas turbine TBCs, Yttria-Stabilized Zirconia (YSZ), cannot be used in temperature higher than 1200˚C, and it degrades when in contact with impurities arise from low quality fuels such vanadium and sulfur. Higher efficiency and performance of gas turbine engines will require a new generation of thermal barrier coatings (TBCs). In this work, some new candidates for replacing YSZ are studied. The focus on finding new candidates is divided in to two main categories; I: replacing zirconia based TBCs with new ceramic materials with different structures, II: stabilizing zirconia with other oxides instead of Yttria. The research focus is on the hot corrosion behavior of $Gd_2Zr_2O_7$, ZrO_2 stabilized with Ta_2O_5 and zirconia stabilized with both Ta_2O_5 and Y_2O_3.

To prepare TBC samples using plasma spray coating, nickel-based superalloy (Inconel 738) disks of Φ25×1.5 mm were employed as the substrates. TBCs composed of a ceramic top coating and a NiCrAlY bond coat (Amdry 9625, Sulzer Metco, with particle size 45~75 µm) were deposited onto the superalloy substrates by the atmospheric plasma spray (APS) process. For example, TBC top coats, YSZ, 50 wt% YSZ+50 wt% $Gd_2Zr_2O_7$and $Gd_2Zr_2O_7$, were made in one of our studies using agglomerated powders. The plasma spraying was carried out using a Sulzer-Metco 9M plasma spray system using an Ar/H_2 gas mixture. The spraying parameters are given in Table 2.1.

Table 2.1. Plasma spraying parameters

Layer	Arc current (A)	Coating distance (mm)	Plasma gas Ar/H_2 (SCFH)	Carrier gas Ar (SCFH)	Powder feed rate (g/min)
Bond coat	500	130	96/15	8	40
Ceramic layer	660	80	64/32	8.4	40

The experimental methods on the hot corrosion study of zirconium tantalum oxides are reported in the following paragraph. Similar approaches were used to study other TBC samples.

Hot corrosion studies using Na_2SO_4 and V_2O_5 mixtures were conducted on samples at 1100˚C in air. For the above mixtures, 95% Na_2SO_4 and 99.9% V_2O_5 from Sigma Aldrich were used. Five types of ceramic samples, YSZ, 70 wt%ZrO_2 + 30 wt% Ta_2O_5 (30TaSZ), 70 wt% YSZ + 30 wt% Ta_2O_5 (30TaYSZ), 50 wt%ZrO_2 + 50 wt% Ta_2O_5 (50TaSZ), and 30 wt%ZrO_2 + 70 wt% Ta_2O_5 (70TaSZ) were made using agglomerated powders from Sigma Aldrich. To obtain the samples, powders were first pressed with binders in a uniaxial die (2.5 cm inner diameter) at 350 MPa pressure to obtain the compressed green bodies, which were then sintered at 1450˚C for 5 hours and 30 minutes to obtain the dense bodies. To perform an accelerated high-temperature hot corrosion test on samples, a mixture of 50wt% Na_2SO_4 + 50wt% V_2O_5 deposit was spread evenly onto the surfaces of the specimens with a mixed salt amount of 20 mg/cm^2. The specimens were then set in an electric furnace with an ambient atmosphere under a maximum temperature of 1100˚C for 4 h. The furnace has two small holes for air to flow naturally. After each 4 h of testing at 1100˚C, the samples were allowed to cool down inside the furnace, and then the samples were inspected both visually and with an optical microscope for possible crack initiation. To repeat the test, the samples were recoated with the Na_2SO_4 + V_2O_5 salt mixture and the heating profile was repeated. The morphology and microstructure of the as received samples and the samples after the hot corrosion tests were examined using field emission scanning electron microscopy (Quanta3D FEG, FEI Company, USA). For surface morphology studies using SEM, a thin Pt layer was sputtered onto the samples to improve the electrical conductivity. X-ray diffraction (MiniFlex XRD, Rigaku Corporation, Japan) with Cu Kα radiation $\lambda = 1.54178$ Å at a scan speed of 1˚/min was used to establish the phase composition of the specimen.

The dislocation dynamics texture study was conducted at LBNL by adding radial shear stress to the DAC loaded sample. The Fit2D and MAUD software were used to process the texture data. The Figure 2.1 below shows a typical synchrotron high pressure shear stress texture measurement experiment setup.

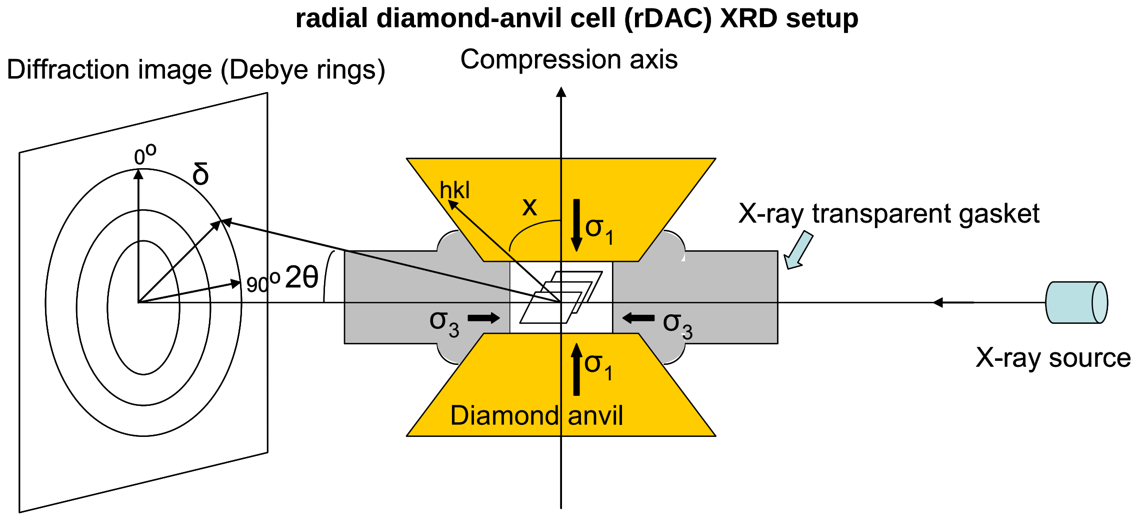

Fig 2.1 The radial synchrotron x-ray diffraction shear stress texture measurement setup.

3. Results and Discussions:

3.1: For the evolution of hot corrosion resistance of YSZ, $Gd_2Zr_2O_7$, and $Gd_2Zr_2O_7$+YSZ composite thermal barrier coatings, the following results were found.

Figure 3.1.1 reveals the X-ray diffraction patterns for the as-received conventional YSZ, $Gd_2Zr_2O_7$+YSZ, and $Gd_2Zr_2O_7$ coatings. It can be seen that the major phase of the APS coated YSZ is tetragonal zirconia, $Gd_2Zr_2O_7$+YSZ coating includes both tetragonal ZrO_2 and $Gd_2Zr_2O_7$ phases, and $Gd_2Zr_2O_7$ has a single phase as expected. The cross-sectional microstructure of APS YSZ, $Gd_2Zr_2O_7$+YSZ and $Gd_2Z_2O_7$ TBC specimens are shown in Fig. 3.1.2. All layers of the as-sprayed specimens have similar microstructures with a noticeable level of porosity without any visible cracks. For the as-sprayed TBC samples, no delamination can be found along the YSZ / $Gd_2Zr_2O_7$+YSZ / $Gd_2Zr_2O_7$ top layer and the NiCrAlY bond coat interface. Figure 3.1.3 shows the XRD patterns obtained from the YSZ, $Gd_2Zr_2O_7$+YSZ, and $Gd_2Z_2O_7$ coatings after the hot corrosion test with the Na_2SO_4+V_2O_5 salt mixture at 1050ºC. Comparing the patterns of the as-sprayed TBC samples, most of the tetragonal zirconia in the YSZ sample has changed to the monoclinic phase and YVO_4 is formed as a hot corrosion product, while for the other two specimens, besides monoclinic ZrO_2 the newly evolved peak is related to $GdVO_4$.

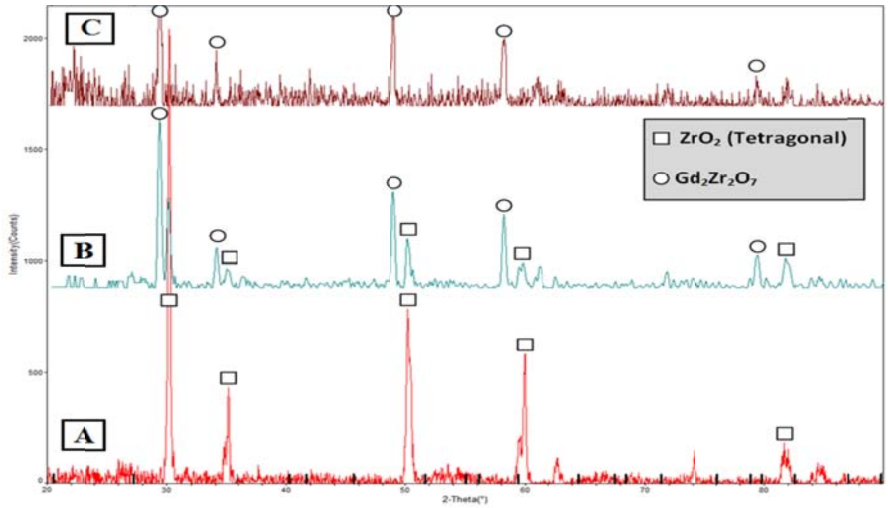

Fig 3.1.1. XRD patterns of as-received A) conventional YSZ, B) $Gd_2Zr_2O_7$+YSZ, C) $Gd_2Zr_2O_7$

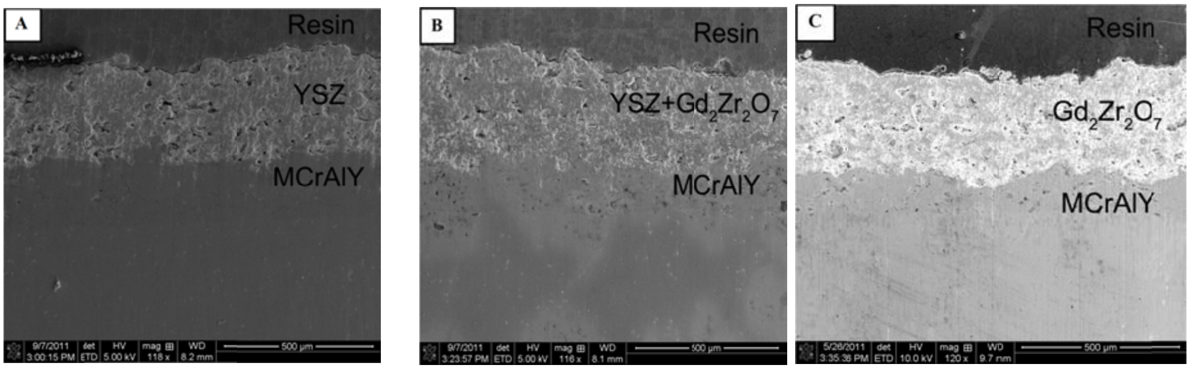

Fig 3.1.2. Cross-section of APS coatings A) conventional YSZ, B) $Gd_2Zr_2O_7$+YSZ, C) $Gd_2Zr_2O_7$

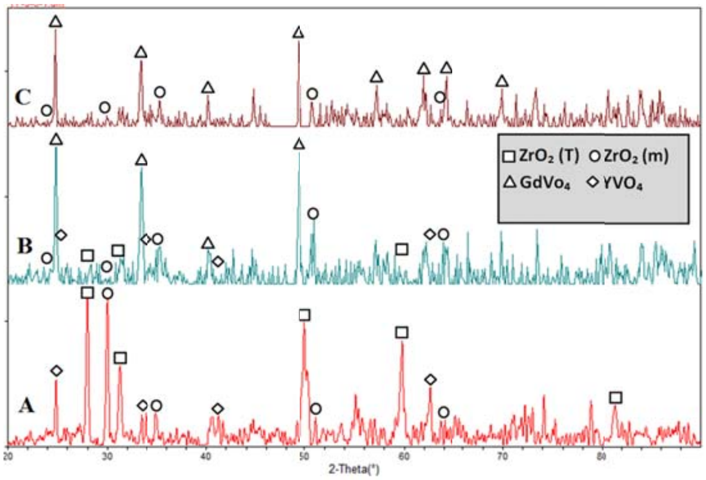

Fig 3.1.3. XRD patterns of A) conventional YSZ, B) $Gd_2Zr_2O_7$+YSZ, C) $Gd_2Zr_2O_7$ after hot corrosion in Na_2SO_4+V_2O_5 at 1050 ºC

Typical surface morphologies of YSZ, $Gd_2Zr_2O_7$+YSZ and $Gd_2Zr_2O_7$ specimens after hot corrosion tests are presented in Fig. 3.1.4, with the apparent formation of new crystals. Apart from XRD analysis, Fig.3.1.3, Energy Dispersive Spectroscopy (EDS) analysis, Fig.3.1.5, was performed at different regions of the TBC surfaces to confirm the chemical compositions of the hot corrosion products. EDS analysis from region A on Fig. 3.1.4a demonstrated that the crystals were composed of yttrium, vanadium and oxygen, then they were identified by XRD analysis to be YVO_4. The EDS spectra obtained at different regions of A and B in Fig. 3.1.4c confirmed the presence of elements consistent with the formation of $GdVO_4$ (region A) and existence of $Gd_2Zr_2O_7$ (region B). For Gd_2VO_4 specimen, small amount of zirconium coming from the background was also detected (Fig. 3.1.5c).

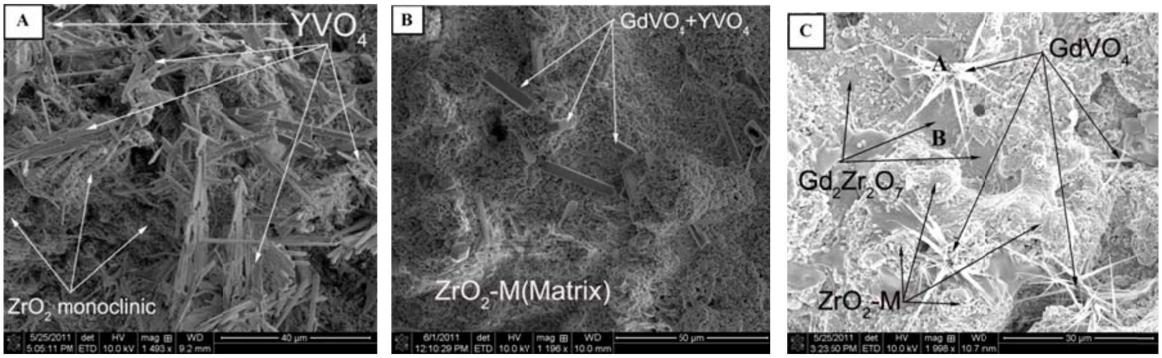

Fig 3.1.4. SEM surface images of A) conventional YSZ, B) $Gd_2Zr_2O_7$+YSZ, C) $Gd_2Zr_2O_7$ after hot corrosion in $Na_2SO_4+V_2O_5$ at 1050ºC

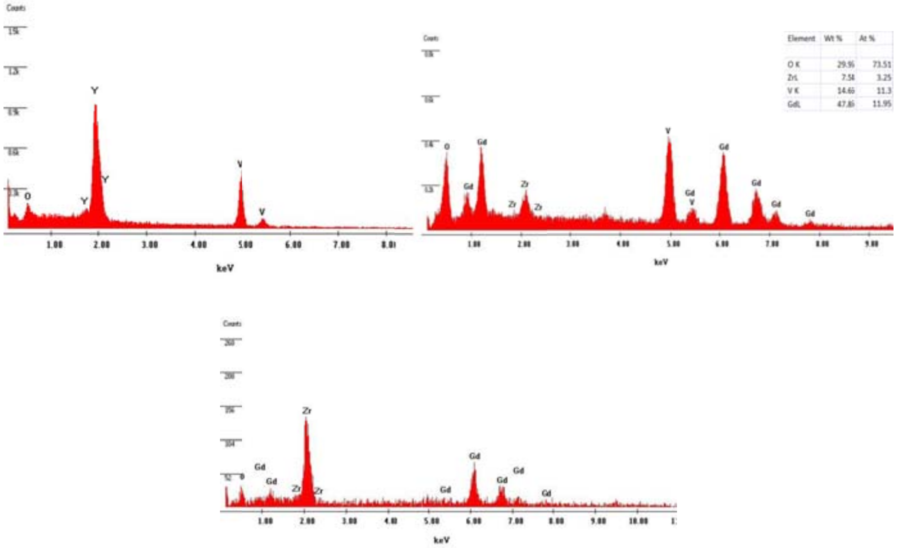

Element	Wt %	At %
O K	29.95	73.51
ZrL	7.54	3.25
V K	14.65	11.3
GdL	47.86	11.95

Fig 3.1.5. EDS spectra from the surface of the coatings A) crystal at region A in Fig. 3.1.4a, B) crystal at region A in Fig. 3.1.4c, C) region B in Fig. 3.1.4c

For the conventional YSZ TBC coating, after hot corrosion tests for 20 hours at peak temperature of 1050°C (five 4-hours cycles), serious degradation and spallation started to occur, Fig. 3.1.4a. Due to the damage by the Na_2SO_4+V_2O_5 corrodents, a porous layer was formed on the YSZ coating. Phase analysis results on these porous areas showed that a large amount of tetragonal zirconia on the surfaces of the conventional YSZ top layer had transformed to monoclinic phase due to the depletion of yttria. In addition, large quantity of rod shaped hot corrosion reaction product, YVO_4, was detected on the surface of the conventional YSZ coating. Similar findings have been reported by other researchers.

For the $Gd_2Zr_2O_7$+YSZ and $Gd_2Zr_2O_7$ coating, the corrosion products are $GdVO_4$ and YVO_4 as well as monoclinic ZrO_2. In Fig.3.1.4B, it is obvious that some regions are perfectly intact and the major phase in these areas is $Gd_2Zr_2O_7$. Compare to YVO_4, the $GdVO_4$ crystals are much smaller in size and quantity and they have a unique dendrite shape. For the YSZ sample, after hot corrosion tests, large quantity of rod shaped YVO_4 crystals are visible on the coating surfaces.

After exposure to molten salt at 1050ºC for 20 hours (five 4-hours cycle), spallation and delamination started to occur in conventional YSZ coating. Chemical degradation of conventional YSZ coatings can be classified as successive occurrence of related chemical reactions during the hot corrosion tests. During the exposure of V_2O_5 and Na_2SO_4 salt mixture at a high temperature (1050°C), a new compound of $NaVO_3$ will be formed.

$$V_2O_5 + Na_2SO_4 \rightarrow 2\,(NaVO_3) + SO_3 \qquad (3.1.1)$$

Then, $NaVO_3$, having a melting point of 610 °C, reacts with yttria from the YSZ solid solution to form YVO_4:

$$ZrO_2\,(Y_2O_3) + 2(NaVO_3) \rightarrow ZrO_2 + 2(YVO_4) + Na_2O \qquad (3.1.2)$$

Also Na_2O can react with V_2O_5 directly to form $NaVO_3$:

$$Na_2O\text{ (base)} + V_2O_5\text{ (acid)} = 2NaVO_3\text{ (salt)} \qquad (3.1.3)$$

The molten $NaVO_3$ is also reported to increase the atom mobility, hence further promote the depletion of yttria from YSZ and the growth of YVO_4 crystals. The Kinetic of reaction (3.1.2) is controlled by the mobility the Y^{3+} in the lattice which migrate preferentially toward the reaction interface due to the high V concentration present on the coating surface. After losing Y_2O_3, the transformation of tetragonal zirconia to monoclinic zirconia during the cooling stage of thermal cycling is accompanied by 3-5% volume expansion, leading to cracking and spallation of TBCs.

The $Gd_2Zr_2O_7$+YSZ and $Gd_2Zr_2O_7$ coatings started to degrade after 36 hours (nine 4-hours cycles) of hot corrosion testing. For comparison, microscopic observations and phase analysis has been done after the same duration of hot corrosion testing as for YSZ (five 4-hours cycles). Exposure of the $Gd_2Zr_2O_7$+YSZ and $Gd_2Zr_2O_7$ coatings to the molten mixture of Na_2SO_4+V_2O_5 at 1050ºC, after hot corrosion tests for five 4-hours cycles at peak temperature of 1050°C, results in additional peaks on XRD measurements attributed to $GdVO_4$ and monoclinic ZrO_2. As described earlier, if Na_2SO_4 and V_2O_5 react and $NaVO_3$ forms then, the possible reactions that would have produced these phases can be written as:

$$Gd_2Zr_2O_7(s) + 2NaVO_3\,(l) \rightarrow 2GdVO_4(s) + 2ZrO_2\text{ (monoclinic)} + Na_2O \qquad (3.1.4)$$

$$Gd_2O_3(s) + 2NaVO_3\,(l) \rightarrow GdVO_4(s) + Na_2O \qquad (3.1.5)$$

No evidences from the XRD patterns indicate direct chemical interactions between Na_2SO_4

with YSZ and $Gd_2Zr_2O_7$, thus the chemical reactions between Na_2SO_4 and YSZ and $Gd_2Zr_2O_7$ are believed to be minimum at the elevated temperature of 1050ºC, which has also been reported by other researchers.

V_2O_5 may also react with $Gd_2Zr_2O_7$ directly at elevated temperature to form $GdVO_4$, monoclinic ZrO_2 or ZrV_2O_7.

$$3V_2O_5\,(l) + Gd_2Zr_2O_7(s) \rightarrow 2ZrV_2O_7(s) + 2GdVO_4(s) \qquad (3.1.6)$$

$$V_2O_5\,(l) + Gd_2Zr_2O_7(s) \rightarrow 2GdVO_4(s) + 2ZrO_2\ (\text{monoclinic}) \qquad (3.1.7)$$

Based on XRD analysis, both $GdVO_4$ and monoclinic ZrO_2 are found in the hot corrosion products of the $Gd_2Zr_2O_7$ coatings; thus reactions (3.1.4) and (3.1.7) are believed to be the main mechanisms for the degradation of $Gd_2Zr_2O_7$ coatings.

It has been reported that $GdVO_4$ crystals can be produced by the reaction of $Gd_2Zr_2O_7$ and $NaVO_3$ at a temperature as low as 600°C. The production of $GdVO_4$ consumes V_2O_5 and thus postpones the formation of YVO_4 crystals and consequently less monoclinic ZrO_2 and less YVO_4 crystals are formed. This is believed to be the main mechanism for the improved hot corrosion resistance for the $Gd_2Zr_2O_7$+YSZ composite coating. On the surface of the YSZ+$Gd_2Zr_2O_7$ composite coating, YVO_4 crystals have a small rod shape (about 20 µm in length), which is significantly smaller than the large rod shaped YVO_4 found in the conventional YSZ coatings (about 50 µm in length). The presence of fine-grained $Gd_2Zr_2O_7$ around YSZ particles also reduces the direct contact of conventional YSZ with molten salt, thus a better corrosion resistance. For pure YSZ coatings, YVO_4 forms throughout the entire thickness of the coating, apart from the stresses induced by the ZrO_2 phase transfer due to the reduction of Y_2O_3, as foreign objects, the corrosion product (YVO_4) could impose extra stresses, which can easily initiate cracks and damage the coating. The smaller the YVO_4 size, the lower the stresses and thus a better durability. For the YSZ+$Gd_2Zr_2O_7$ composite coating, after 36 hours of accelerated hot corrosion test, many regions in the YSZ+$Gd_2Zr_2O_7$ composite coatings are still intact and the original tetragonal ZrO_2 phases exist. Clearly, YSZ+$Gd_2Zr_2O_7$ composite coating provides better resistance against hot corrosion than the conventional YSZ. In the $Gd_2Zr_2O_7$ case, the corrosive area is small with isolated dendritic shaped $GdVO_4$ crystals. Also many surface regions are still intact with the original $Gd_2Zr_2O_7$ phase. Unlike the YSZ case, where the hot corrosion attacks the stabilizer Y_2O_3, which has a small quantity in nature, the hot corrosion attacks the bulk $Gd_2Zr_2O_7$ layer, thus the $Gd_2Zr_2O_7$ coating provides a better resistance against hot corrosion than the conventional YSZ.

Hot corrosion of ceramic oxides against molten salt such as V_2O_5 and $NaVO_3$ is mostly controlled by Lux-Flood type of acid-base reactions and are explainable in terms of the relative acid-base character of the oxide. The severity of the reactions increases as the relative acidity to basicity between the reactants increases. There is no direct information about the relative basicity of rare-earth zirconates in the open literature; however, we could estimate the basicity from the respective metal oxides. Rare earth oxides such as Sm_2O_3, Yb_2O_3, Gd_2O_3 are more basic than Y_2O_3 therefore, it will react at lower vanadium (or vanadium oxide) activities. On the other hand, as reflected from the thermodynamic data, $GdVO_4$ is more stable than YVO_4, which indicates that a higher V_2O_5 or $NaVO_3$ activity is required for $GdVO_4$ formation than for YVO_4 formation. In this experiment, $Gd_2Zr_2O_7$ is less basic than YSZ which means that the driving force of reaction (3.1.2) is larger than that of reaction (3.1.4) thermodynamically. Besides, the better hot corrosion immunity of $Gd_2Zr_2O_7$ might be favored by kinetic factors, such as dissolution kinetics. Because the dissolution process usually involves two steps: dissociation of the compound into ions or atoms and the subsequent diffusion of these ions or atoms into the melt. Consequently, the dissolution kinetics may be affected by the interface dissociation, the diffusion in the melt, or both of them.

The representative cross section SEM images of the conventional YSZ, $Gd_2Zr_2O_7$+YSZ and $Gd_2Zr_2O_7$ coatings after the hot corrosion tests are presented in Fig. 3.1.6. As shown in Fig. 3.1.6(a), the corroded areas near the YSZ/bond coat interface implies a weak coating which can be easily torn off; large harmful horizontal cracks have formed inside the conventional YSZ layer throughout the thickness of coating. Transverse cracks are clearly visible in the YSZ coating, Fig. 3.1-6a. In certain regions, the cracks divided the YSZ layer into several sub-layers, implying the initiation of delamination and spallation of the YSZ coating. Some large cracks have propagated and extended deep into the ceramic coat and even reached the top-coat/bond-coat interface, which would be susceptible to cause the debonding of the ceramic coat from the bond coat. Moreover, comparing Fig. 3.1.2a and Fig. 3.1.6a, the thickness of YSZ layer has been reduced after hot corrosion test. YSZ tetragonal to monoclinic phase transformation initiated from the beginning of hot corrosion test. As it accompanied by volume expansion, it can be tore off easily by small thermal and mechanical shocks during the hot corrosion cycles. So the failure of YSZ coating may occur by gradual loss of YSZ coating from the surface toward bond coat. This means, the thickness of YSZ layer should be reduced after hot corrosion test.

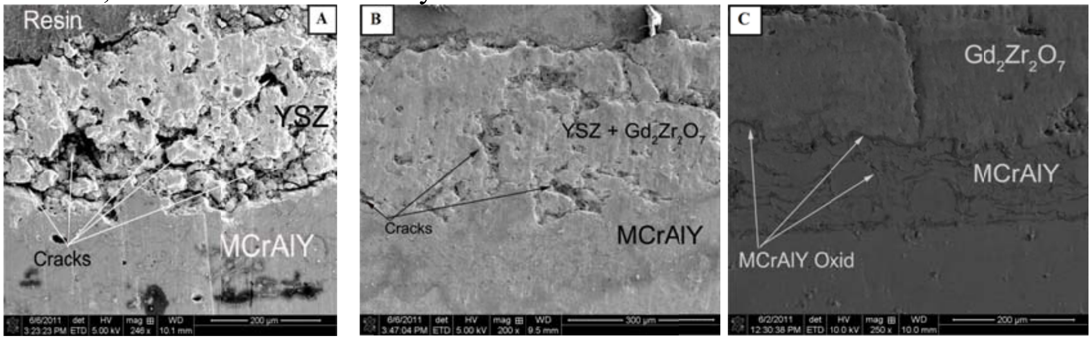

Fig 3.1.6. Cross-section of A) conventional YSZ, B) $Gd_2Zr_2O_7$+YSZ, C) $Gd_2Zr_2O_7$ after hot corrosion in $Na_2SO_4+V_2O_5$ at 1050 ºC

The micro cracks and pores were observed in both conventional YSZ and YSZ+$Gd_2Zr_2O_7$ coatings. In comparison, the YSZ+$Gd_2Zr_2O_7$ coating has finer and fewer micro cracks than the conventional YSZ coating. In the case of YSZ+$Gd_2Zr_2O_7$ composite coatings, only a few visible cracks were observed inside the zirconia layer after the hot corrosion test but without spallation. It can be concluded that molten salts and oxygen penetration were retarded in this specimen thus a better hot corrosion resistance.

Fig. 3.1.6C shows a $Gd_2Zr_2O_7$ coating cross-section, which has no significant degradation and spallation after hot corrosion test. Although one vertical-crack appears from the surface to bond coat, no visible degradation around the tip of the crack is observed. The cross-section image of the $Gd_2Zr_2O_7$ coating shows less porosity than the conventional YSZ which means it's harder for the molten salts and the oxygen to penetrate through the $Gd_2Zr_2O_7$ layer. This further confirms that the $Gd_2Zr_2O_7$ coating exhibits a good hot corrosion resistance and good durability.

Fig. 3.1.7 shows the crack of a delaminated YSZ coating. The infiltration of molten salt through the entire YSZ coating leads to the formation of dendritic YVO_4 crystals throughout the entire thickness of the crack. The formation of YVO_4 crystals implies the depletion of Y_2O_3 in this region, which leads to the subsequent tetragonal to monoclinic ZrO_2 transformation and thus a large destructive volume changes/stresses within the ceramic coat.

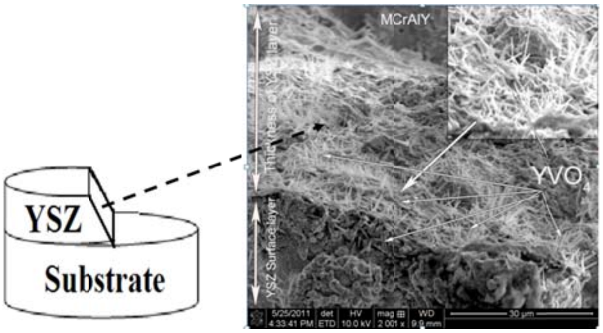

Fig 3.1.7. Cross section along the crack of a delaminated YSZ coating after hot corrosion in $Na_2SO_4+V_2O_5$ at 1050 ºC

3.2: Phase stability and hot corrosion behavior of ZrO_2-Ta_2O_5 compound, the following results were found.

In this study, five types of ceramic samples, YSZ, 70 wt%ZrO_2 + 30 wt% Ta_2O_5 (30TaSZ), 70 wt% YSZ + 30 wt% Ta_2O_5 (30TaYSZ), 50 wt%ZrO_2 + 50 wt% Ta_2O_5 (50TaSZ), and 30 wt%ZrO_2 + 70 wt% Ta_2O_5 (70TaSZ) were made using agglomerated powders from Sigma Aldrich.

Figure 3.2.1 depicts the X-ray diffraction patterns for the as-received YSZ, 30TaSZ, 50TaSZ and 70TaSZ specimens. In Fig. 3.2-1A, for sintered YSZ, only diffraction peaks corresponding to tetragonal ZrO_2 can be distinguished. In the 30TaSZ, a mixed tetragonal and orthorhombic phases form, and 50TaSZ sample shows a near pure orthorhombic phase of zirconium tantalum oxide. The zirconium tantalum compound in orthorhombic phase is found to be $TaZr_{2.75}O_8$, based on the XRD patterns of 30TaSZ and 50TaSZ. For 70TaSZ sample, besides $TaZr_{2.75}O_8$, well-defined peaks corresponding to Ta_2O_5 are also observed. Note in Fig. 3.2.1, the more intense peaks of Ta_2O_5 are at $2\theta = 22.8°$ and 28.3°.

Figure 3.2.2 shows the as-received SEM image of YSZ, 30TaSZ, 50TaSZ and 70TaSZ. These SEM images show a typical microstructure of pressed and sintered samples with certain amount of porosity, visible on the surface of samples. In Fig. 3.2-2D, for 70TaSZ sample, there are two distinct microstructures, a matrix of orthorhombic $TaZr_{2.75}O_8$ and some isolated Ta_2O_5 regions. This sample is made of 30 wt. % of ZrO_2 mixed with 70 wt. % of Ta_2O_5.

Figure 3.2.3 illustrates XRD patterns of YSZ, 30TaSZ, 50TaSZ and 70TaSZ specimens after hot corrosion at 1100˚C in $Na_2SO_4+V_2O_5$ salt for 40 hours (10 cycles). In Fig. 3.2.3A, starting from tetragonal phase, after 40 hours of tests, a large portion of the YSZ sample changed to the monoclinic phase by the $Na_2SO_4+V_2O_5$ salt. YVO_4 is formed as the major hot corrosion product.

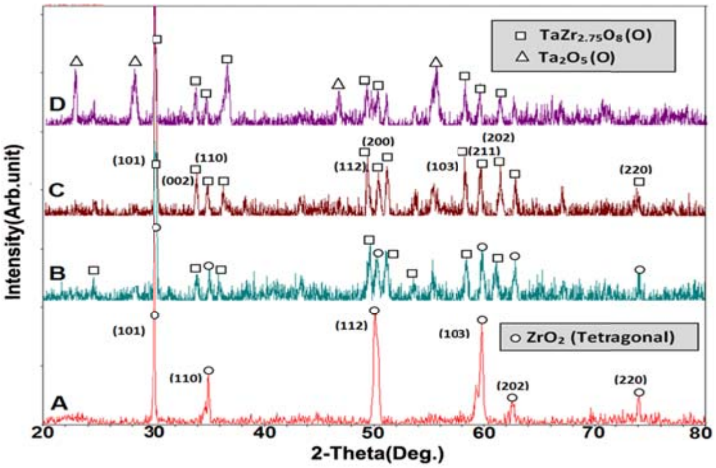

Fig 3.2.1. XRD patterns of as-received A) YSZ, B) 30TaSZ, C) 50TaSZ and D) 70TaSZ

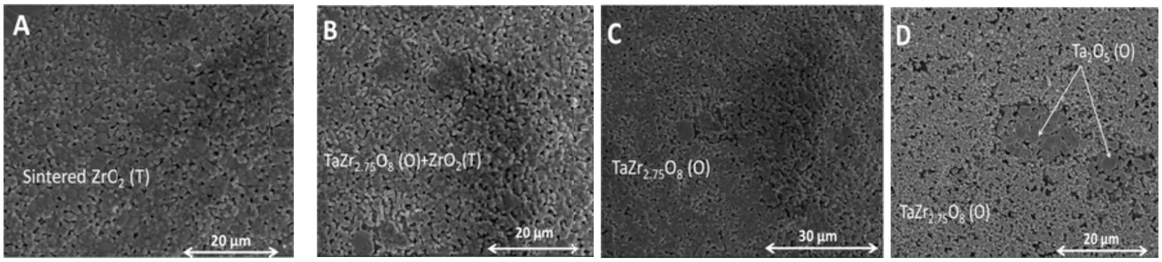

Fig 3.2.2. SEM images of as-received sintered A) YSZ, B) 30TaSZ, C) 50TaSZ and D) 70TaSZ

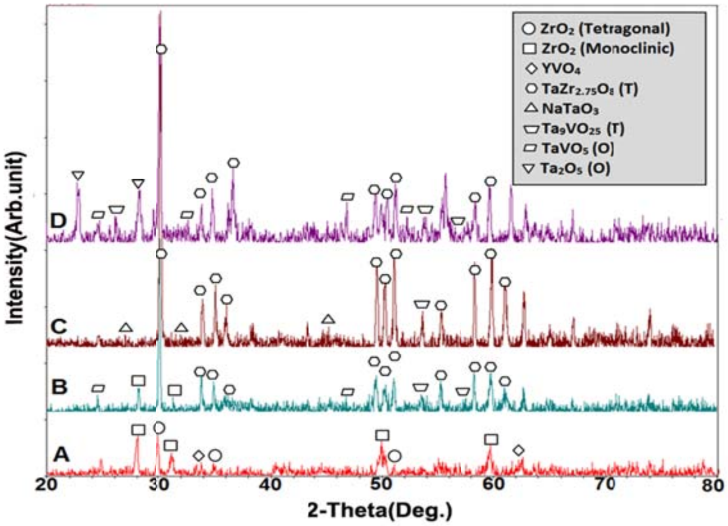

Fig 3.2.3. XRD patterns of A) YSZ, B) 30TaSZ, C) 50TaSZ and D) 70TaSZ after hot corrosion in $Na_2SO_4 + V_2O_5$ at 1100˚C for 40 hours

An examination of XRD pattern of the 30TaSZ sample, besides $TaZr_{2.75}O_8$ and tetragonal zirconia peaks which are present in the original as-received sample, after hot corrosion, some new peaks are identified which can be contributed to monoclinic zirconia, $TaVO_5$ and Ta_9VO_{25}. SEM images of the YSZ, 30TaSZ, 50TaSZ and 70TaSZ specimen after hot corrosion tests are presented in Fig. 3.2.4. Apart from XRD analysis (Fig. 3.2.3), Energy Dispersive Spectroscopy (EDS) analysis was performed at different regions of the samples to confirm the chemical compositions of the hot corrosion products. For crystals in Fig. 3.2.4A, EDS analysis demonstrated that these crystals were composed of yttrium, vanadium, and oxygen. Further analysis confirmed these crystals were YVO_4. Hot corrosion products of 30TaSZ sample are rod-shape. The extent of the attack is, however, much smaller in comparison to the YSZ sample.

In the 50TaSZ case, after hot corrosion, only a small quantity of rod-shaped crystals was formed. According to EDS result, crystals in Fig. 3.2.4C contain sodium, tantalum and oxygen and with considering the XRD pattern, they are found to be $NaTaO_3$. Most of the $TaZr_{2.75}O_8$ surface didn't react with molten salt and it is almost perfectly intact. XRD shows strong peaks of orthorhombic phase of zirconium tantalum oxide.

In 70TaSZ sample, besides TaV_9O_{25}, strong peaks contributed to pure Ta_2O_5 and $TaVO_5$ were also detected, Fig. 3.2.3D. The formation of considerable amount of $TaVO_5$ and Ta_9VO_{25} crystals in this sample is due to the large amount of excess Ta_2O_5, which reacts with the molten salt. Considering the intensity of the XRD peaks and the amount of hot corrosion products, reaction rate of 70TaSZ is higher than the 50TaSZ case. However, exposure to Na_2SO_4+V_2O_5 salt does not cause destabilization of zirconium tantalum oxide to monoclinic phase seen for the YSZ sample.

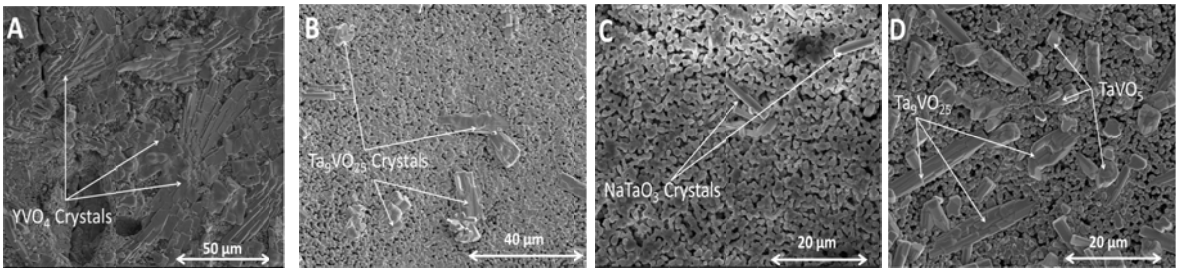

Fig 3.2.4. SEM surface images of A) YSZ, B) 30TaSZ, C) 50TaSZ, D) 70TaSZ after hot corrosion in Na_2SO_4 + V_2O_5 at 1100 ˚C for 40 hours.

It is noteworthy to compare the hot corrosion behavior of 30TaYSZ (30 wt. % Ta_2O_5+70 wt. % YSZ) with 30TaSZ (30 wt. % Ta_2O_5+70 wt. % ZrO_2). Figure 3.2-5 shows the XRD patterns of the as-received 30TaYSZ and 30TaSZ. As indicated by the XRD patterns, 30TaYSZ is a pure tetragonal zirconia phase while 30TaSZ is a mixture of tetragonal zirconia and orthorhombic tantalum zirconium oxide ($TaZr_{2.75}O_8$). For 30TaYSZ, the amount of Ta_2O_5 added into YSZ is not high enough to form complex tantalum zirconium oxide. Instead, tetragonal zirconia is found to be the only phase formed, with Ta_2O_5–Y_2O_3 dopants in the ZrO_2 matrix. Similar findings are reported in previous studies.

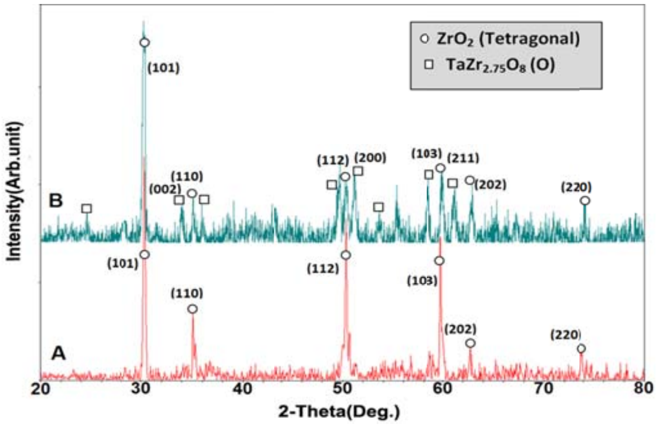

Fig 3.2.5. XRD patterns of as-received A) 30TaYSZ, B) 30TaSZ

Figure 3.2.6 shows XRD patterns of 30TaYSZ and 30TaSZ specimens after hot corrosion at 1100˚C in Na_2SO_4+V_2O_5 salt for 40 hours. In Fig. 3.2.6A, it is seen that the 30TaYSZ sample, which is pure tetragonal to begin with, has high level of monoclinic phase, in conjunction with the formation of YVO_4, due to Na_2SO_4+V_2O_5 salt corrosion. Besides orthorhombic $TaZr_{2.75}O_8$ and tetragonal zirconia, some new peaks are identified on 30TaSZ sample after hot corrosion, which are monoclinic zirconia, $TaVO_5$ and Ta_9VO_{25}. Figure 3.2.7 shows SEM images of 30TaYSZ and 30TaSZ after hot corrosion at 1100˚C in Na_2SO_4+V_2O_5 salt for 40 hours. Based on the quantity of corrosion products, 30TaSZ is found to have a better hot corrosion resistance than 30TaYSZ, due to the formation of the highly stable orthorhombic $TaZr_{2.75}O_8$ phase.

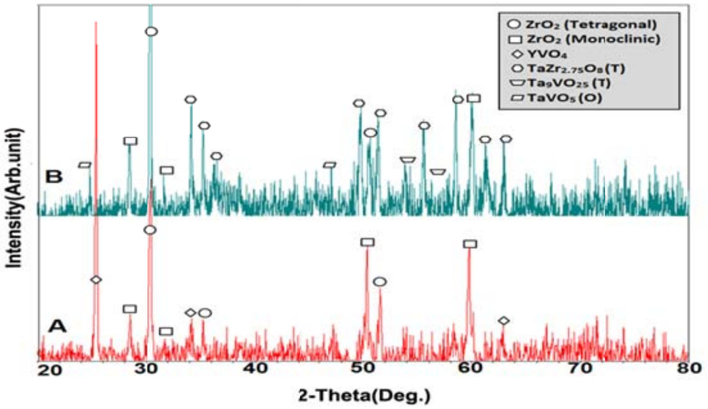

Fig 3.2.6. XRD patterns of A) 30TaYSZ, B) 30TaSZ after hot corrosion in Na_2SO_4 + V_2O_5 at 1100 ˚C for 40 hours

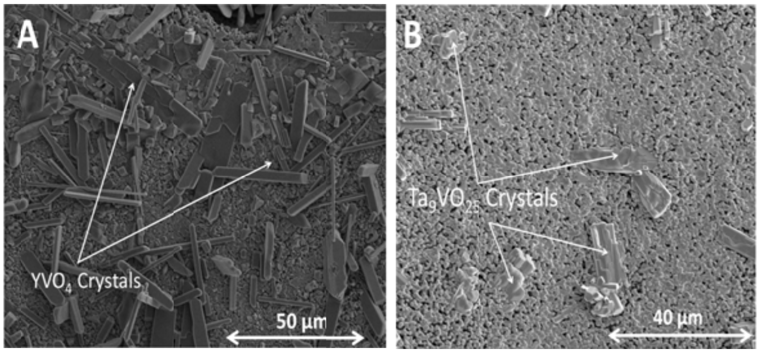

Fig 3.2.7. SEM surface images of A) 30TaYSZ, B) 30TaSZ, after hot corrosion in Na_2SO_4 + V_2O_5 at 1100 ˚C for 40 hours.

Comparing all samples tested in this study, hot corrosion resistance of 50TaSZ is the best. This sample has a near single orthorhombic phase of $TaZr_{2.75}O_8$, which is highly stable in high temperatures and resistant to hot corrosion attack in molten salts.

3.3: High pressure synchrotron XRD experiments

In experiment part, we also trained students and postdocs on dislocation dynamics synchrotron XRD texture experiment and data processing. The experiment was performed at LBNL beamline 12-2-2. The systems studied include pure Ni, NiS, multi-component alloys, and $Gd_2Zr_2O_7$ etc.

Based on the high pressure synchrotron XRD experiments, under room temperature, mechanical milling prepared alloy Cr-Y keeps a stable structure up to at least 39 GPa. We performed first principles simulation and confirmed our experimentally determined mechanical properties [Ref. 3]. Then MD simulation was performed and the Y and Ta dopant effects were analyzed. At high temperature the Y and Ta dopants forming stable Y and Ta oxide to shield the corrosion and buffer the thermal stress between hot and cool TBC parts. To include specific Cr in the bond coat sample preparation, mechanical alloying is a promising method.

3.4: Simulations:

We have screened out three types of bond coats for using at three different temperature ranges: (1). at T < 950 degree C, Cr-Y-Ta (with concentration 3%~6% Y & Ta) is a potential candidate; (2). at T = 1,000 ~ 1,200 degree C, Ir-Ta-Al is a potential candidate; and (3). at T > 1,200 degree C, we may use composition of Hf-Mo-Nb-Ta-Ti-Zr (1:1:1:1:1:1) as one of the potential bond coat candidates. Our MD computer simulation confirmed the structure stability. To be applied in practical products, the long term bond coat/top coat stability tests in both simulation and experiment are needed.

In top coat study, we simulated the relative stability of several top coat systems. We performed *ab initio* DFT based electronic structure simulations to obtain the relevant thermodynamic data.

For 30TaSZ, 50TaSZ and 70TaSZ, section 3.2, Na_2SO_4 and V_2O_5 would first react and form $NaVO_3$, then, the possible reactions that would have produced those identified reaction products include:

$$\text{TaSZ } (Ta_2O_5)(s) + NaVO_3(l) \rightarrow NaTaO_3(s) + TaVO_5(s) \qquad (3.4.1)$$

$$\text{TaSZ } (5Ta_2O_5)(s) + NaVO_3(l) \rightarrow NaTaO_3(s) + Ta_9VO_{25}(s) \qquad (3.4.2)$$

In this study, there are many unusual substances, such as $TaVO_5$, Ta_9VO_{25}, whose thermodynamic data cannot be found easily. We checked several common handbooks, databases and software packages, such as the CRC Handbook of Chemistry and Physics, the Bureau of Mines and USGS database, the NIST-JANAF Thermochemical Tables, the MatNavi NIMS Materials Database, the HSC Chemistry package etc and failed to obtain useful information. A literature search also failed to generate the required complete thermodynamic data set. To further assist the understanding of the corrosive reactions, we performed *ab initio* density functional theory (DFT) based electronic structure simulations to obtain the relevant thermodynamic data. The Gibbs free energy of formation was calculated for each reactant and product by summation the energy of formation at 0K, zero point energy, vibrational internal energy and free energy at 1227 ˚C, and PV term. The phonon module in the software MedeA was used to calculate the thermodynamic vibration parameters. The (VASP) was used to perform DFT calculations where plane wave basis set was implemented. The *ab initio* projector augmented wave (PAW) general gradient approximation (GGA) calculation method with plane wave basis sets was used and 400 eV plane wave cut-off energy was set in the simulation. Each lattice in all of the supercells was selected to be larger than ~ 7 Å. Only harmonic vibration approximation was considered in the phonon calculations. The calculated Gibbs free energy of formation results are shown in Table 3.4.1.

Table 3.4.1: At 1500K, Gibbs free energy of formation in unit kJ/mol:

Substance	Y_2O_3	$NaVO_3$	YVO_4	Na_2O	Ta_2O_5	$NaTaO_3$	$TaVO_5$	Ta_9VO_{25}
Gibbs Energy	-2713.24	-1501.93	-3960.34	-494.51	-1719.71	-1304.14	-2048.53	-10693.86

For $NaTaO_3$, the Gibbs free energy of formation at 1500K is -1304.14 kJ/mol, while the Gibbs free energy of formation for $TaVO_5$ at 1500K is -2048.53 kJ/mol. To make a comparison, the Gibbs free energy of formation of YVO_4 at 1500K is -3960.34 kJ/mol. So, YVO_4 is much more stable than both $NaTaO_3$ and $TaVO_5$. Since Na_2O has a low melting temperature of 1132 ˚C, the Y_2O_3 and YVO_4 can be easily dissolved in Na_2O. Also Na_2O can further feed the formation of $NaVO_3$. All these explain the experimentally observed fast reaction of Y_2O_3 than Eqs. 3.4.1 and 3.4.2.

Based on the calculated Gibbs free energy results, all experimentally observed stability and reaction date are well explained. We had also performed MD simulation on $TaZr_{2.75}O_8$ crystal. The simulation results show a stable $TaZr_{2.75}O_8$ supercell at temperature up to 1050 K.

4. High Temperature TBC Durability Testing Rig Development and Thermal Cycling testing

4.1 Overview of TBC Testing Rig

There are mainly two test methods for TBCs high temperature properties: the isothermal oxidation test which uses the muffle furnace and cycling test which mostly uses burner rig. The isothermal oxidation test cannot reflect the cycle-dependence of the TBCs properties at high temperature. Although in the burner rig test, the thermal gradient can be produced by using cooling gas from the back of the substrate, the fluctuation of the surface temperature can be huge due to unstable flame, which complexes the analysis of the failure mechanism.

While in the gas turbine engine, TBCs are subjected to not only the high temperature but also the high pressure. Besides, there is thermal gradient along the direction of the coating surface to the metal substrate due to the internal and external gas cooling.

In order to better simulate the TBCs working environment, a novel new test rig was designed and fabricated. The required main functions are:

(1) Heat and keep the TBCs samples as high as 1350 °C for long time;

(2) Provide and maintain the internal pressure as high as 150 psi;

(3) Introduce and control the gas composition constituted as many as four different gases;

(4) Generate the temperature gradient of at least 100 °C between the ceramic surface and the back of metallic substrate and make it measurable;

(5) Automatically control the thermal cycling test and make it programmable;

(6) Real-time monitor and record the failure of samples.

According to the above requirement, the design and fabrication work were initially started by a group of senior students in mechanical engineering department of LSU. They built up the steel vessel which can generate a high pressure inside, the support table where the vessel locates, the gas pipeline to introduce different compositions of gases. After that more than two years have been devoted to accomplish the initial requirements of the test rig through design-build-trouble shouting-redesign procedure. Fig.4.1.1 illustrates the final design of the test rig and Fig.4.1.2 shows the fabricated rig.

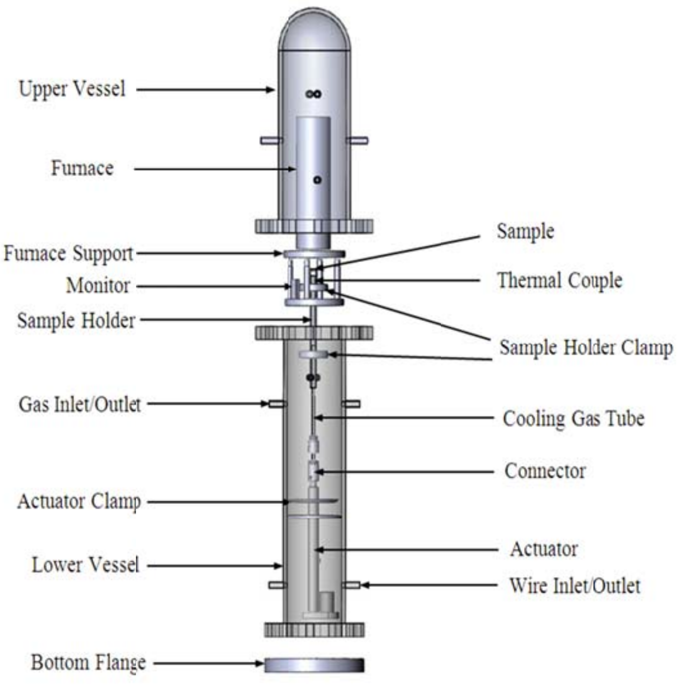

Fig. 4.1.1 Thermal cycling test rig design

Fig.4.1.2 Thermal cycling test rig under construction (L) and under operation in the lab (R)

4.2. High Temperature Function

To achieve the high temperature, the robust radiator from MHI company was used as the heating element (see Fig.4.2.1). The coil heating element is made of molybdenum disilicide and the maximum core temperature is 1900 ^{o}C with a continuous work temperature of 1700 ^{o}C. The coil is first insulated by ceramic refractory and then by insulating fiber to reduce the heat dissipation. The programmable silicon controlled rectifier (SCR) temperature controller from MTI Company is used to control the heating temperature.

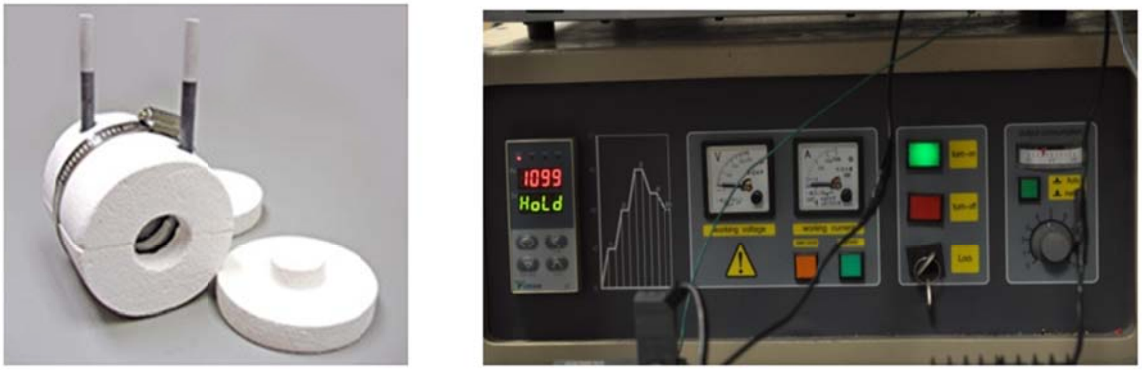

(a) (b)

Fig.4.2.1 robust radiator (L); temperature controller panel (R)

4.3 High Pressure and Various Gas Atmospheres

The high pressure is realized by the upper and lower vessel sealed by spiral wound gasket. Pressure gauge and relief valve were also installed on the external wall of the upper vessel. Mass flow controllers and 4-channel mass flow readout were used for the gas composition control.

4.4 PLC Control

24V DC actuator with potentiometer for position output was used to carry the samples into and out of the furnace (see Fig.4.4.1(a)). The actuator was controlled by a Siemens Program Logic Controller (PLC) (Fig.4.4.1(b)). 24V DC is the main power supply for the PLC and the actuator. A 12V DC power supply was used to transfer the resistance to voltage which is the feedback signal to the PLC.

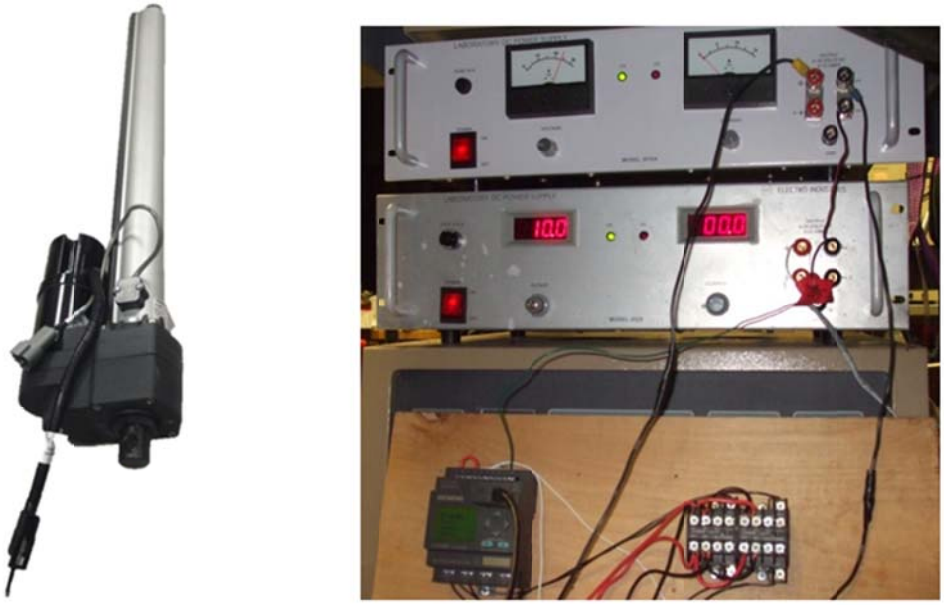

(a) (b)

Fig.4.4.1 (a) Actuator; (b) Siemens Program Logic Controller (PLC) and DC power supply

4.5 Thermal Gradient Design

To generate thermal gradient, the back of the substrate must be cooled by compressed cooling gas. The magnitude of thermal gradient can be controlled by the cooling air flow rate. The temperature of top surface of the sample is the same as the furnace temperature because when running the test, the sample holder stops at the position where the furnace thermocouple is as close as possible to the top surface of the sample. To calculate the thermal gradient, the back temperature of the substrate needs to be known. This is realized by another thermocouple which is put into the cooling tube, see Fig.4.5.1.

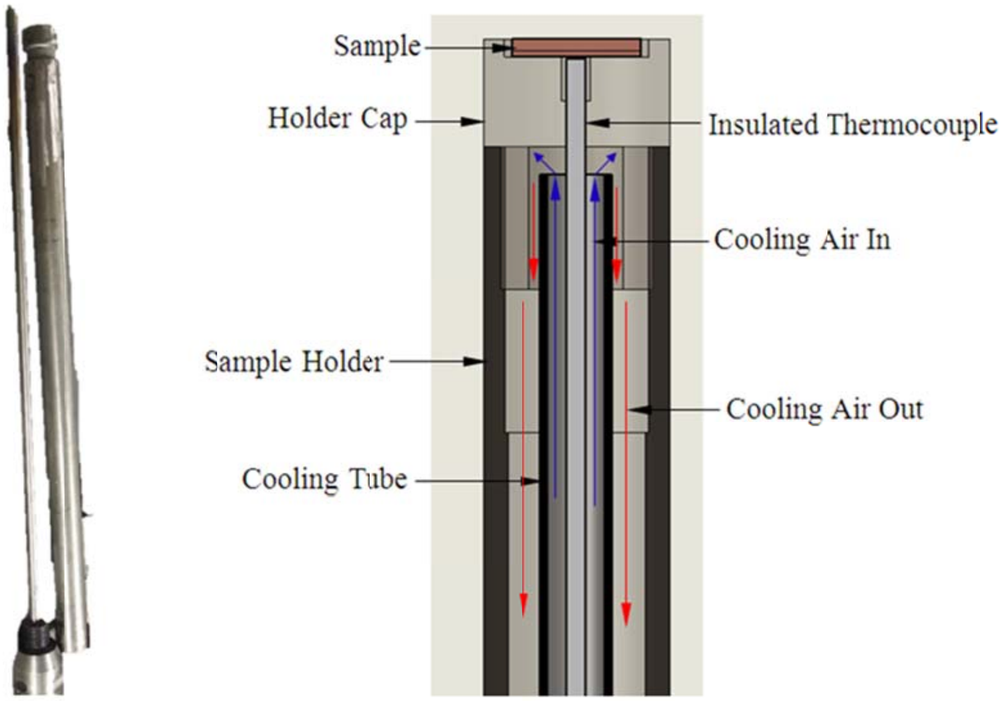

(a) (b)

Fig.4.5.1 (a) Assembled sample holder, cooling tube and thermocouple; (b) Illustration of cooling mechanism

4.6 On-line Monitor for Sample Failure Testing

The TBCs thermal cycling life varies from several hours to a couple of months depends on the materials used and the test conditions. To know when the sample fails is very important especially in the case of a closed environmental test. For example, in the TBCs thermal cycling test with high pressure and different components of gases, it is very arduous to assemble and dissemble the heavy vessel of which the total weight is more than 1,000 pounds. What's more, it is costly to seal the vessel and to use large amount of different gases. Therefore, it is necessary to monitor the failure of sample inside of the vessel.

An auto-focus webcam is used to monitor the failure of the sample when the sample is out of the furnace and gets to the lowest position (see Fig.4.6.1). Because of the strong radiation and convective heat transfer from the high temperature sample, the camera is sealed in a polycarbonate cabin and cooled by the flowing compressed air introduced by the inlet and outlet ports from the bottom of the cabin. Besides the on-line monitor, the camera can record the whole experimental procedure. To save disk space, the camera also can capture and save imagines according to the set time interval.

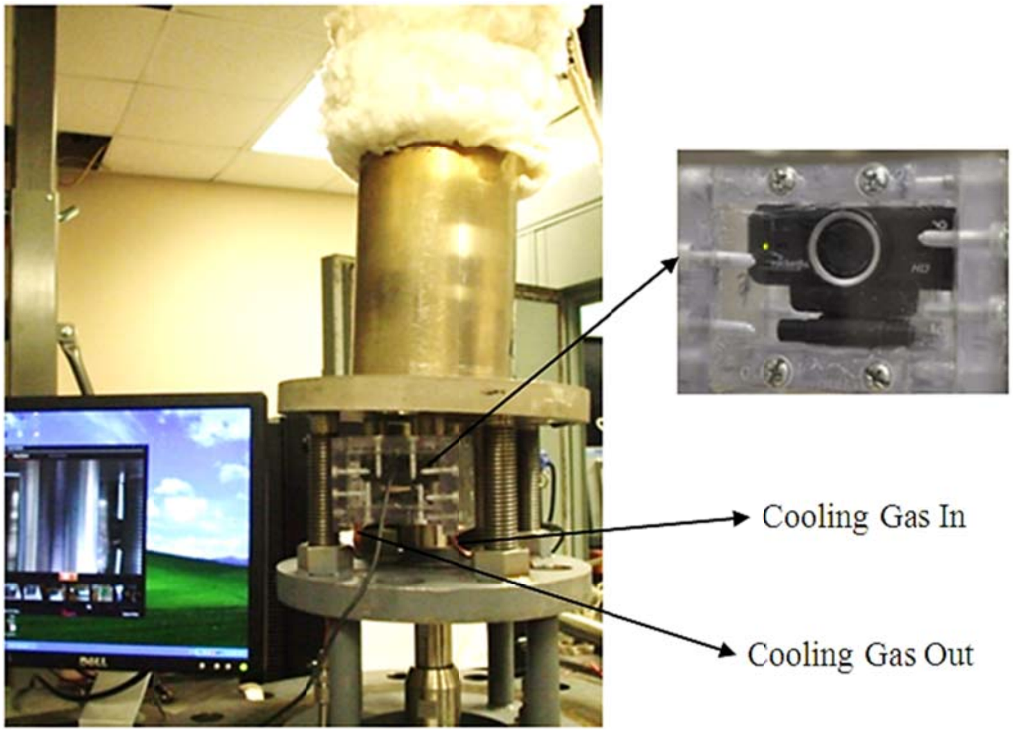

Fig.4.6.1 Camera capturing images while the test in progress

4.7 Thermal Cycling Performances of $Gd_2Zr_2O_7$ Based TBCs

4.7.1 Thermal Cycling of Single and Double Ceramic-layered TBCs

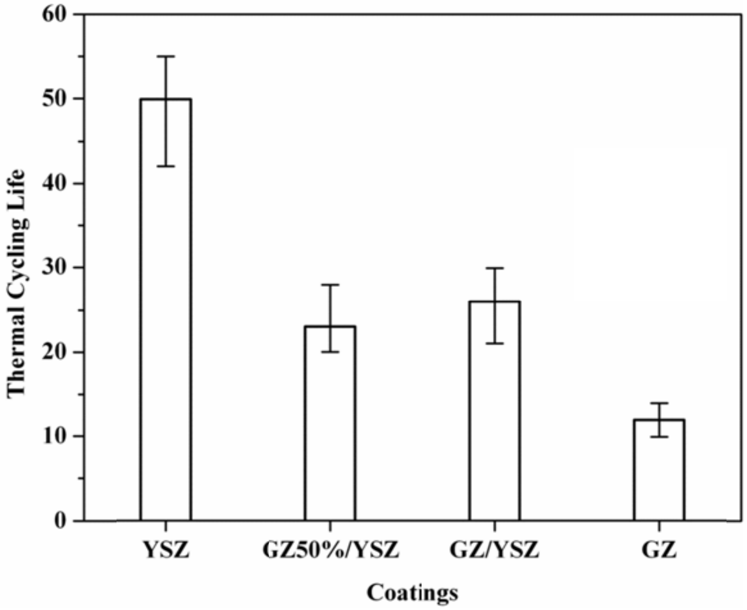

Fig.4.7.1 Thermal cycling life of single and double ceramic-layered coatings at 1150 ºC

Fig.4.7.1 shows the thermal cycling life of the fabricated single and double ceramic-layered coatings. The macroscopic failure appearances are shown in Fig.4.7.2. It can be seen that

YSZ has the longest thermal cycling life. The failure happened by delamination at the edge. GZ failed by complete delamination of the whole ceramic layer and it has the shortest thermal cycling life. Although the thermal expansion coefficient of GZ is close to that of YSZ, it is reasonable to assume that the thermal stress in GZ is larger than that in YSZ considering the sintering effect of GZ. What's more, the fracture toughness of GZ is much lower than that of YSZ, implying that the crack initiation and growth will occur even with lower stress levels. Therefore, the single-layer GZ coating has much lower thermal cycling life than YSZ. GZ50%/YSZ coating failed by bucking, which is another typical phenomenon in YSZ coatings.

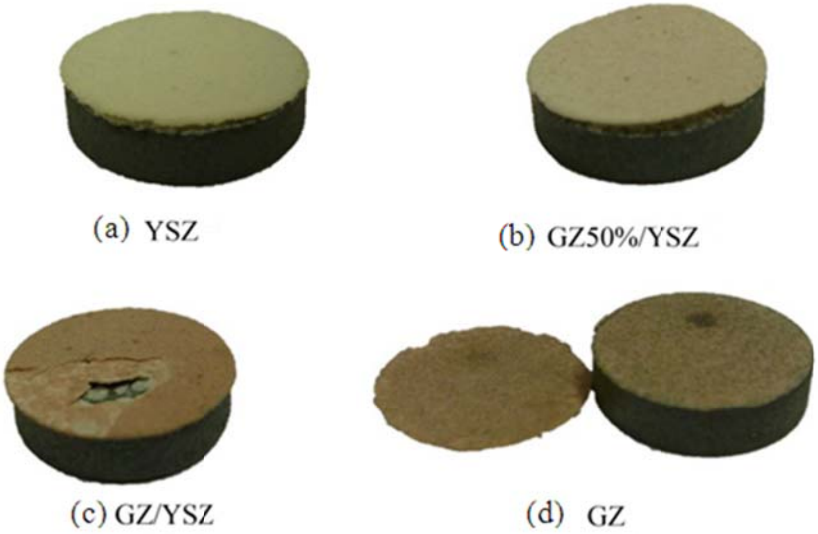

Fig.4.7.2 Photograph of failed single and double ceramic-layered coatings after the thermal cycling test at 1150 ºC. (a)YSZ failed after 31 cycles; (b) GZ50%/YSZ failed after 23 cycles; (c) For GZ/YSZ, the GZ layer was spalled after 26 cycles and after 32 cycles the YSZ were also spalled; (d) GZ failed after 12 cycles.

Fig.4.7.3 displays the SEM micrographs of the cross-section of the failed coatings after thermal cycling. All of them failed in the ceramic layer close to the interface of the YSZ layer and TGO except for GZ/YSZ coatings, leaving spots of ceramics on the surface of the bond coat, which is often occurred in the APS coating systems. Another interesting phenomenon should be noticed is that the ceramic layer often came off in a whole piece within one or two cycles, indicating that large horizontal cracks were initialed and developed into large cracks before the vertical cracks became prominent. This is different from many other results and it may be due to the smaller and edge-unbeveled substrate or more uniform temperature gradient in the furnace cycling test than that in the burner-rig test. In the GZ/YSZ coating the delamination first occurred in the GZ layer close to the interface of GZ and YSZ layers, indicating a different failure mechanism from typical YSZ systems.

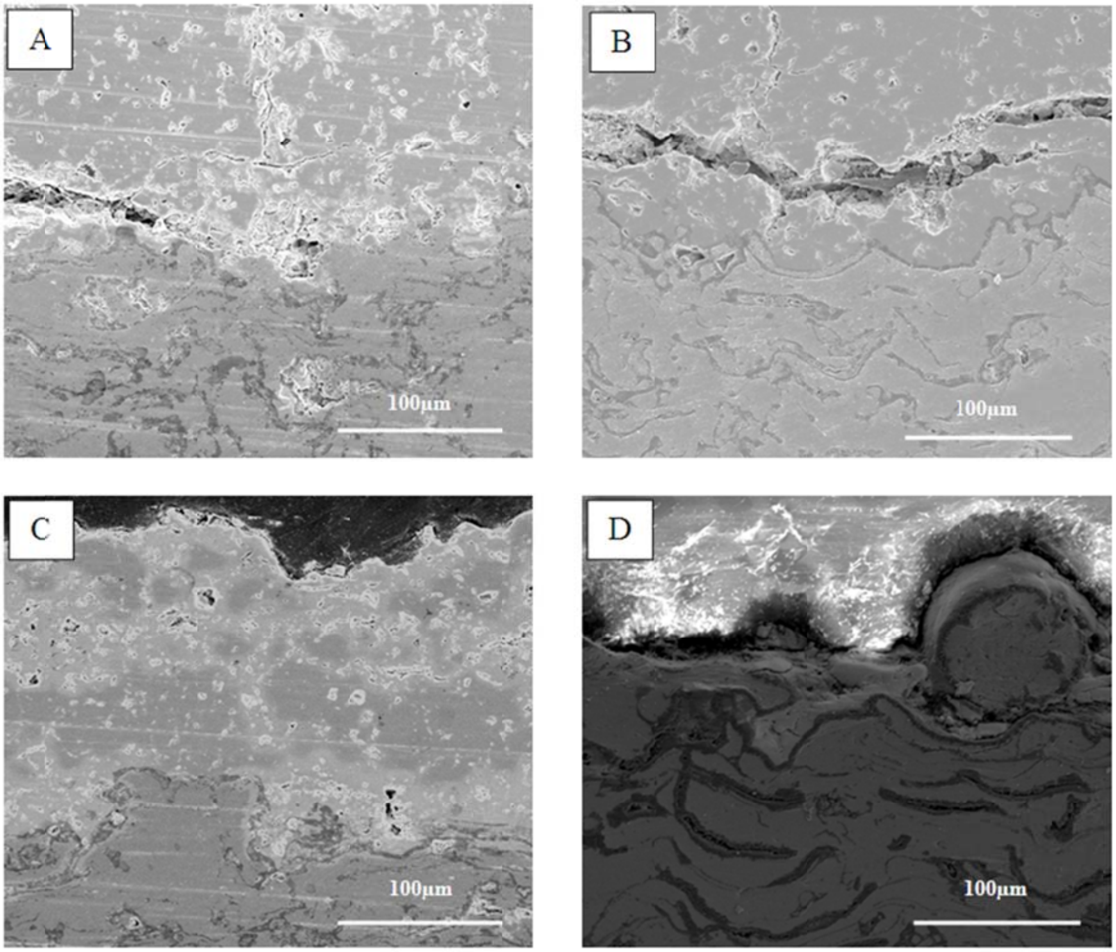

Fig.4.7.3 SEM micrographs of the cross-section of single and double ceramic-layered coatings after thermal cycling tests at 1150 ºC (A) YSZ, (B) GZ50%/YSZ, (C) GZ/YSZ, and (D) GZ.

4.7.2 Thermal Cycling of Three Ceramic-layered TBCs at Different Temperature

Fig.4.7.4 is the measured temperature profile of the 1h-thermal cycling test at 1050 ^{o}C, 1150 ^{o}C, and 1250 ^{o}C. It took around 10 minutes for the specimens to get to the peak temperature. After 10 minutes cooling in the air out of furnace, the temperature was around 260 ^{o}C. The temperature of the specimens was quite stable after they reached to the peak temperature, which is an advantage compared to the burner-rig thermal cycling test.

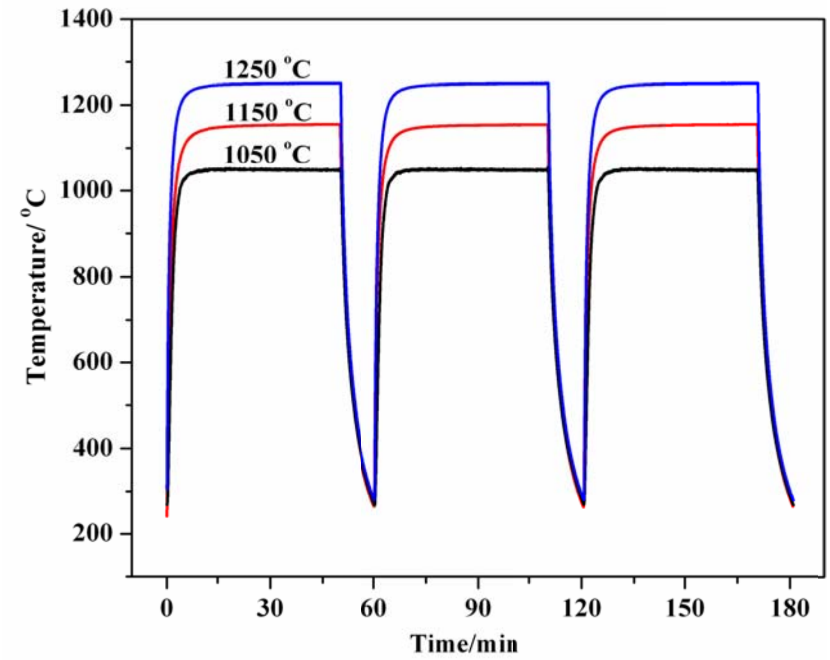

Fig.4.7.4 Measured temperature profile of 1h-thermal cycling test at different temperature using the designed test rig.

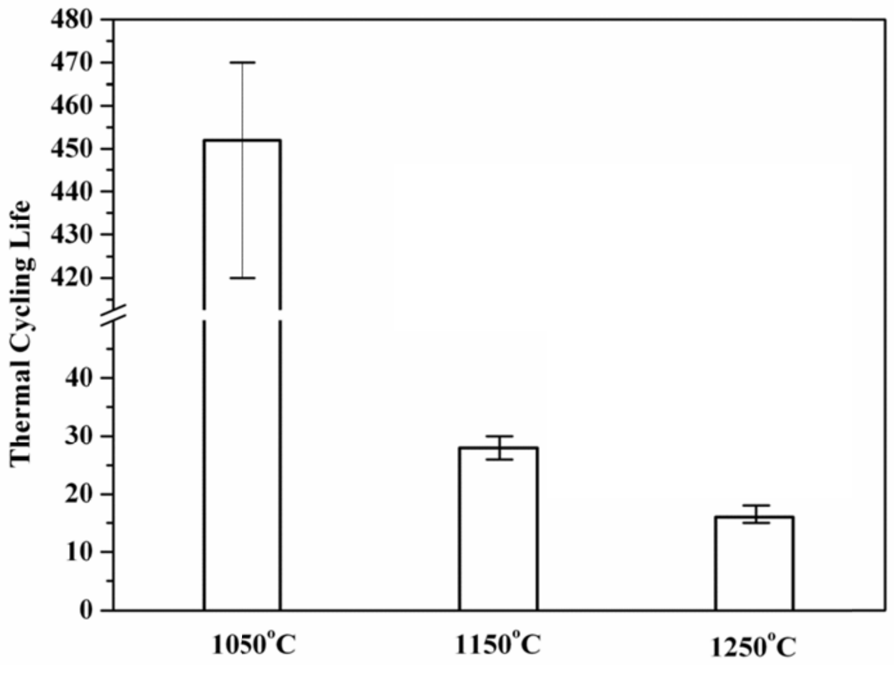

Fig.4.7.5 Thermal cycling life of GZ/GZ50%/YSZ coatings at different temperature with the designed test rig.

Fig.4.7.5 indicates the thermal cycling life of GZ/GZ50%/YSZ coatings at 1050 °C, 1150 °C, and 1250 °C. The macroscopic failure appearances are shown in Fig.4.7.6. It can be seen that the thermal cycling life of coatings was dramatically decreased when the temperature increased from 1050 °C to 1150 °C. Correspondingly, the failure phenomenon was also different. Coatings at 1050 °C failed gradually, first chipped off at the edge of the coating, and then vertical cracks appeared on the surface. Coatings at 1150 °C and 1250 °C failed suddenly, usually within one or two cycles. The failure initiated by the delamination at the edge, and then rapidly grew into large areas. If the vertically crack also grew large enough in the growth process of horizontal cracks, large part of coatings could peel off.

Fig.4.7.6 Photograph of failed GZ/GZ50%/YSZ coatings after the thermal cycling test at different temperature using the designed test rig. (a) Coating failed after 452 cycles at 1050 °C; (b) coating failed after 28 cycles at 1150 °C; and (c) coating failed after 16 cycles at 1250 °C.

Fig.4.7.7 exhibits the SEM micrographs of the cross-section of the failed coatings after thermal cycling at different temperature. In this figure, the delaminated ceramic layers were shown in A, C, and E. There were large vertical cracks along with the horizontal delamination/cracks, which initiated from the top GZ layer. These vertical cracks penetrated into the sub-layer after initiation and may stop by the sub-ceramic layer (as shown in A) or penetrate through the whole ceramic layer (as shown in C and E). The delamination areas around the interface of YSZ layer and the bond coat were shown in B, D, and F. All of the delamination occurred in the YSZ layer close to the interface of the YSZ layer and TGO.

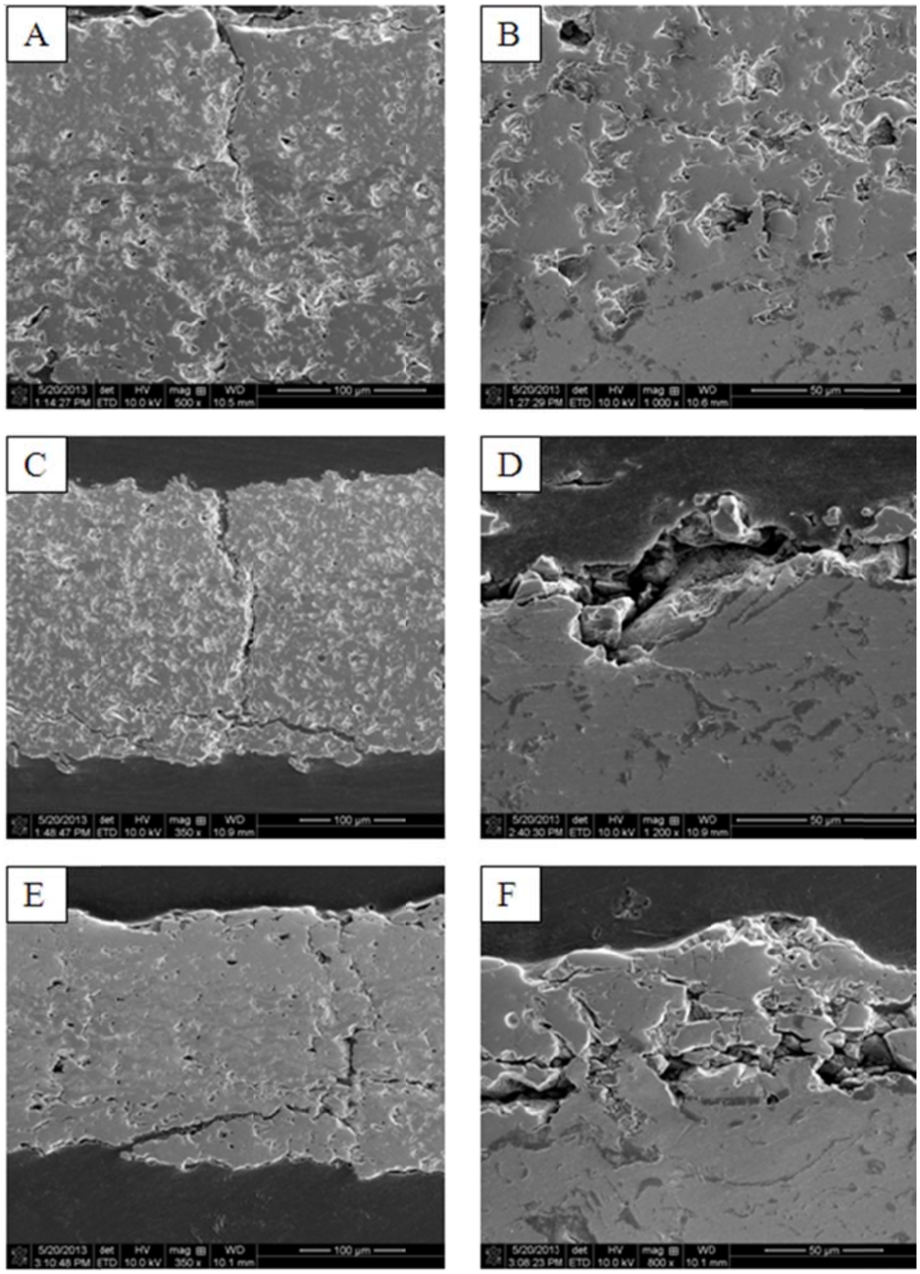

Fig.4.7.7 SEM micrographs of the cross-section of GZ/GZ50%/YSZ coatings after the thermal cycling test at different temperature using the designed test rig. (A) and (B) 1050^{o}C; (C) and (D) 1150^{o}C; (E) and (F) 1250^{o}C.

4.7.3 Thermal Cycling of Three Ceramic-layered TBCs with 10h-thermal-cycling Program

GZ/GZ50%/YSZ coatings experiencing 10h-thermal cycling test failed after 8 cycles, and the macroscopic failure appearances are shown in Fig.4.7.8. The whole ceramic layer was peeled off, leaving ceramic spots on the substrate surface. Also dark spots, the TGO, were observed on the back surface of the delaminated ceramic layer. The microstructure of the front surface of ceramic layer was shown in Fig.4.7.9 A. There were tiny pores between the worm-like GZ grains and micro-cracks showing on the front surface, which increased the in-plane strain tolerance of the ceramic coatings. Therefore, few large cracks showed in the ceramic cross-section microstructure in Fig.4.7.9 D. Dense columnar YSZ grains appeared on the back surface of delaminated ceramic layer (Fig.4.7.9 B). Same morphology was observed on the delaminated surface of the substrate in Fig.4.7.9 C. The cross-section microstructure in E showed no TGO layers which may be lost in the sample-cutting process.

Fig. 4.7.8 Photograph of the failed GZ/GZ50%/YSZ coating after 8 cycles of 10h-thermal-cycling test at 1150 ºC.

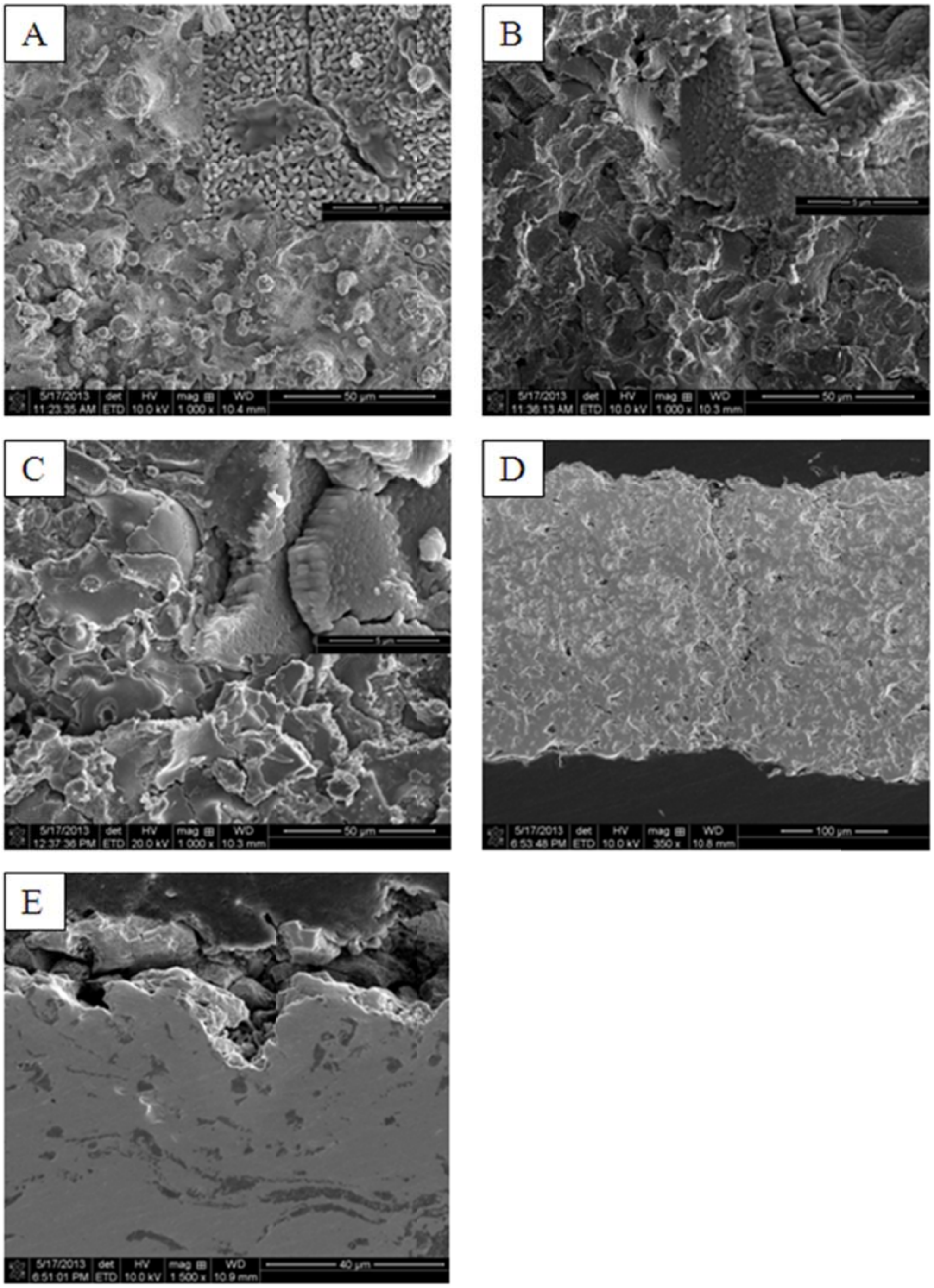

Fig. 4.7.9 SEM micrographs the surface of GZ/GZ50%/YSZ coatings after 8 cycles of the 10h-thermal-cycling test at 1150 ºC.

4.7.4 Thermal Cycling of Double Ceramic-layered TBCs with and without Cooling

Fig.4.7.10 is the measured temperature profile of the 1h-thermal cycling test at 1150 °C with and without cooling. The backside temperature of the substrate was decreased from 1150 °C to 942±2 °C, indicating that there was a ~210 °C thermal gradient in the specimens. The cooling gas also decreased the minimum temperature from ~ 260 ^{o}C to ~133 ^{o}C. The fluctuation of the peak temperature under cooling condition is a litter larger than that without cooling.

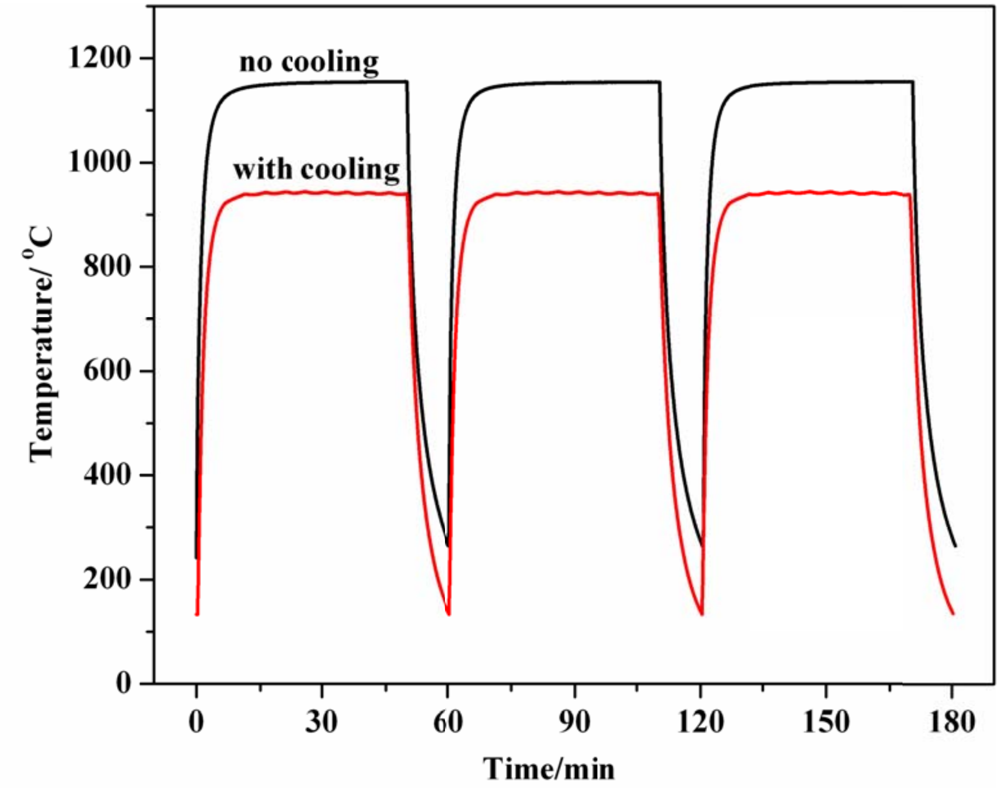

Fig.4.7.10 Measured temperature profile of thermal cycling test at 1150 ^{o}C with and without cooling using the designed test rig.

Fig.4.7.11 indicates the thermal cycling life of GZ/YSZ coatings at 1150 ^{o}C without and with cooling. The macroscopic appearances of coatings are shown in Fig.4.7.12. The thermal cycling life of GZ/YSZ coating with cooling was more than 706. The top surface morphology shown in Fig.4.7.12 (b) indicates that the sample still kept integrity expect for the small chips at the edge. It was not considered to be failed because the damaged area was less than 20%. The dramatic increase of the thermal cycling life with cooling was mainly due to the low temperature of the bond coat. Another thing should be pointed out is the sample size effect. At the same temperature, the thermal cycling life of 1/2" GZ/YSZ samples tested by CM furnace was 26. While for the 1" samples tested in designed test rig, the thermal cycling life was 131. Even considering the differences in test condition, the large samples are considered to have longer thermal cycling life than smaller samples.

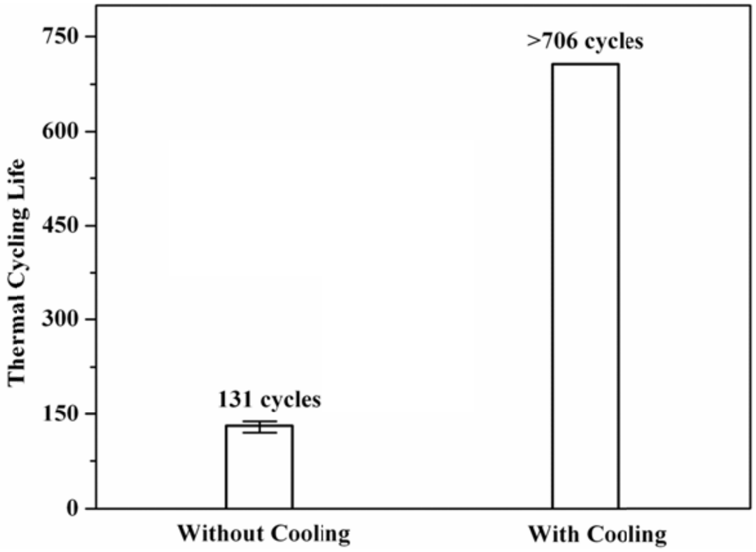

Fig.4.7.11 Thermal cycling life of GZ/YSZ coatings at 1150 ºC without and with cooling using the designed test rig.

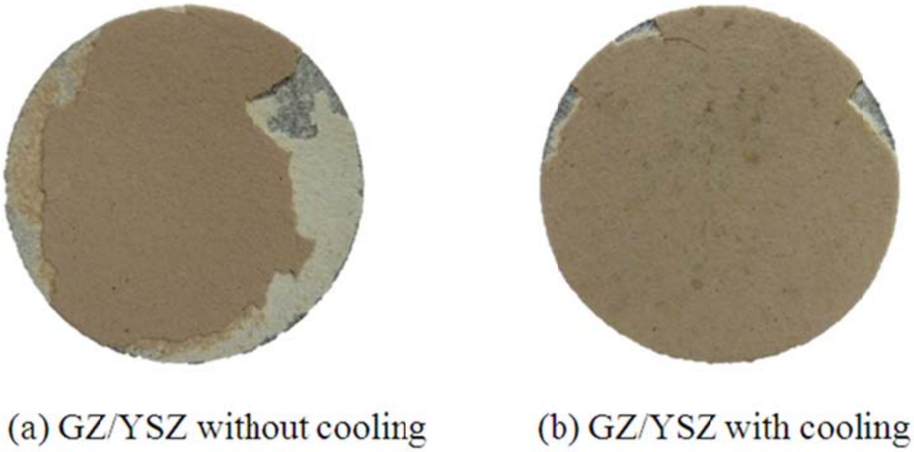
(a) GZ/YSZ without cooling

(b) GZ/YSZ with cooling

Fig.4.7.12 Photograph of GZ/YSZ coatings after the thermal cycling test at 1150 ºC (a) without and (b) with cooling using the designed test rig.

Fig.4.7.13 presented the SEM micrographs of the front surface and cross-section of the coatings after thermal cycling. Without cooling the coating showed lots of cracks on the surface (Fig.4.7.13 A) and big horizontal crack in the YSZ layer close to the top GZ layer (Fig.4.7.13 C). The cracks enhanced the oxidation rate by permitting more oxygen penetrated into the ceramic coating and reached the interface of YSZ/TGO and inside of bond coat. As shown in Fig.4.7.13 C and D, the oxidation of the bond coat without cooling is more severe than that with cooling although the oxidation time is shorter. Also the TGO thickness of coating without cooling (~4.4 μm, Fig.4.7.13 E) is much thicker than that with cooling (~3.4 μm, Fig.4.7.13 F).

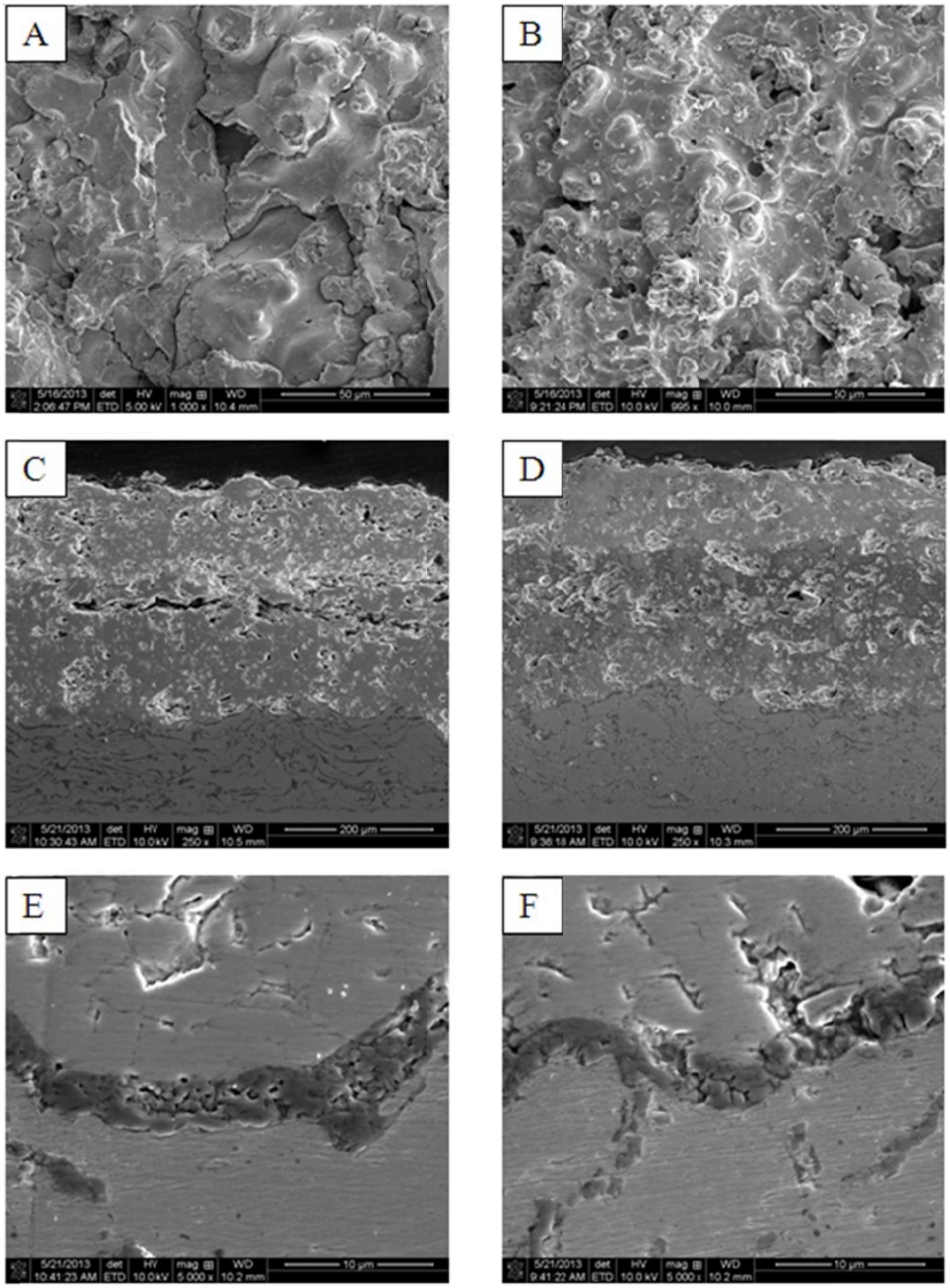

Fig.4.7.13 SEM micrographs of GZ/YSZ coatings at 1150 ºC (A, C, E) without cooling and (B, D, F) with cooling after the thermal cycling test at 1150 ºC.

4.7.5 Failure Mechanism of $Gd_2Zr_2O_7$ Based TBCs

The thermal cycling performances of single, double, and three ceramic-layered GZ based TBCs were carried out under different thermal conditions. The failure phenomenon can be classified into three categories:

(1) Delamination at the edge in YSZ layer close to the YSZ/TGO interface, and further propagation resulted in the entire spallation of the ceramic coating. This is the most phenomenon occurred in the test.

(2) Bucking which only happened in GZ50%/YSZ coating in 1150 ^{o}C thermal cycling test.

(3) Spallation at/close to the interface of two ceramic layers, which occurred in GZ/YSZ two ceramic-layered coatings.

Edge and buckle-driven delamination were also the two main competing failure mechanisms for conventional YSZ TBCs. The same explanation is supposed to be applied for the current GZ based TBCs. P. K. Wright et al. proposed a failure map representing the basic elements of this competition, as shown in Fig.4.7.14. In the lower left of the map, as the TGO experiences large in-plane compressions upon cooling, the film attempts to alleviate the stress by lengthening itself, through out-of-plane displacements. This can happen by TGO bucking. Because the low in-plane modulus of the TBC does not resist the small scale TGO buckling, the system would fail by TBC bucking. In the upper right, the TBC has relatively high in-plane stiffness and limited strain tolerance, causing the residual stress in the TBC to be large and resulting in a high strain energy density. The TGO growth and the increased amplitude of undulations with thermal cycle enhance this energy density which provides a strong driving force for the edge delamination. The plasma sprayed TBC has splat grain morphology and inter splat boundaries parallel to the interface, which makes the relatively in-plane stiffness high, thus most of the failure occurs by edge delamination.

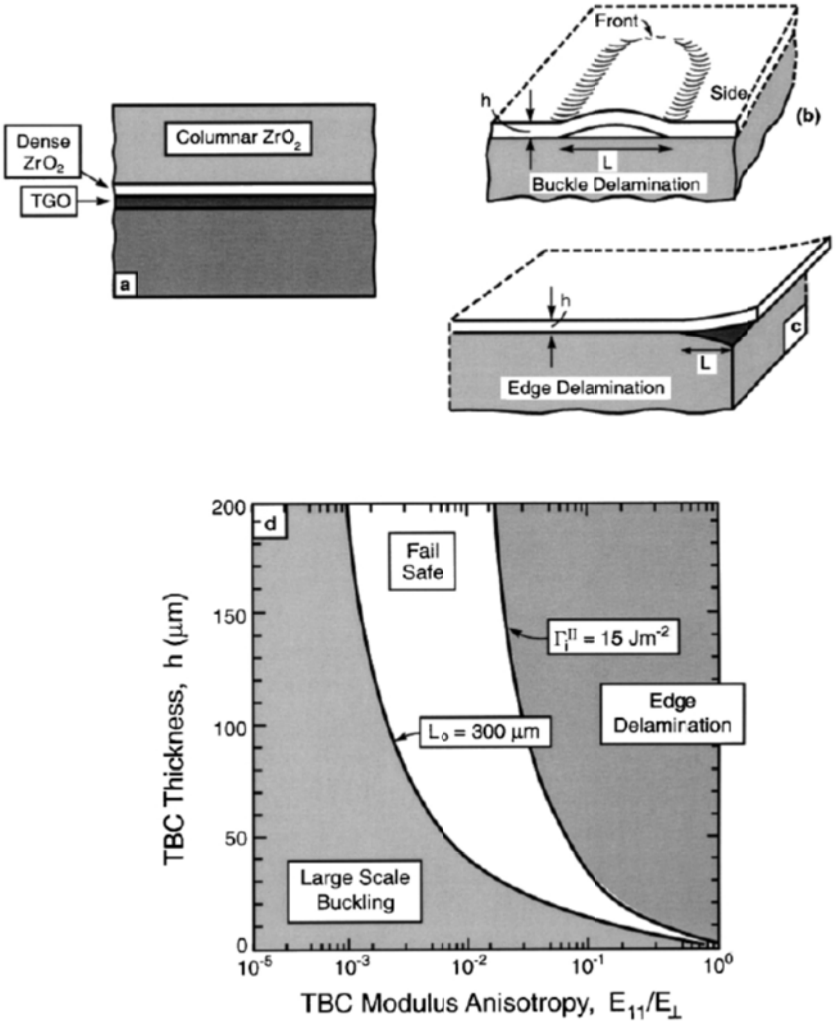

Fig.4.7.14 A schematic of large scale bucking and edge delamination of TBCs with a failure mechanism map.

Above analysis indicates that understanding stresses in the TGO is crucial to analyze the failure mechanism of TBCs. There are two main sources of stresses: (1) one is from the TGO growth at high temperature. Oxidation is accompanied by growth strains and associated stresses. The strain represents the overall volume increase upon converting the alloy to Al_2O_3. The associated stresses comprise in-plane stress which is induced by the lateral growth strain and normal stress which is induced by the out of plane thickening strain due to the formation of new TGO at the interface with the bond coat. Experimental measurements indicated that the TGO growth stresses are compressive and relatively small, ranging from 0 to 1 GPa, because the misfit induced by growth is relaxed by rapid creep in the TGO at high temperature; (2) the other is from the thermal expansion misfit between the ceramic coat and the metal bond coat/substrate upon cooling. Thermal expansion misfit stresses are also compressive, ranging from 3 to 6 GPa.

Imperfections (especially undulations) cause the thermal expansion misfit stresses to redistribute, as shown in Fig.4.7.15. Normal tensions exist where the TGO is convex and vice versa. Shear stresses exist at inclined section. These stresses depend on the elastic mismatch and the ratio of the amplitude to the wavelength of the undulations.

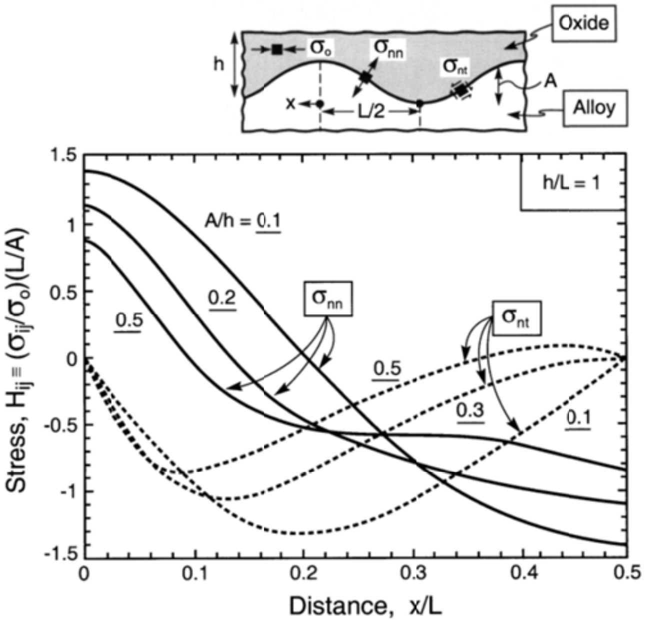

Fig.4.7.15 Distribution of stresses at an undulating TGO interface

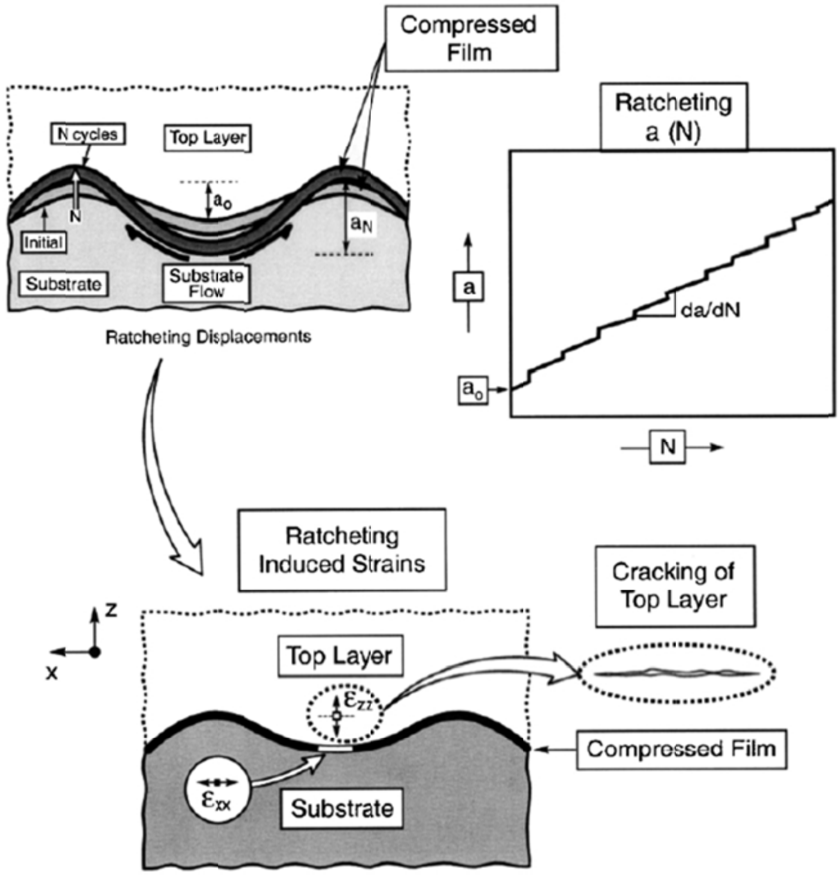

Fig.4.7.16 Schematic indicating the ratcheting phenomenon and its effect

When the shear stresses induced in the bond coat upon cooling sufficiently exceed its yield stress, the bond coat flows plastically from the base to the peak of the prominent undulations, allowing the amplitude to increase (Fig.4.7.16). For the undulation to continue to enlarge, the growth strain at high temperature “feeds” the process. In such cases, steady-state ratcheting becomes possible, whereby the amplitude increases with each thermal cycle.

As the amplitude increases, normal stresses develop in the superposed TBC. The normal stresses govern crack growth parallel to the interface, near the TGO, and they increase systematically as the TGO growth. Upon cooling, the compression normal to the TGO interface diminishes, because of thermal expansion misfit. In fact, should the bond coat creep sufficiently during TGO growth, these stresses become tensile at ambient and motivate interfacial separation.

The failure process of TBCs occurs through a sequence of crack nucleation, propagation and coalescence events. It is motivated by the strain energy density in the TGO and resisted by the fracture toughness along the delamination plane. When the tensile stresses around the undulations are large enough to exceed the delamination toughness of the TBC, cracks are initiated. The TGO growth and increase of the amplitude of undulations enhance the normal tensile stresses which motivate the propagation of cracks. When small cracks become large enough to satisfy buckling requirements, opening of the interface crack faces increases the energy release rate, resulting in a minimum value, which represents a buckle propagation criticality. The coalescence of these cracks results in a separation large enough to satisfy large scale buckling and spalling. Therefore, TBC fails.

With extensive thermal cycling, combinations of thermal expansion misfit and growth strains enlarge the imperfections by a ratcheting mechanism, amplifying the energy release rates and accelerating failure.

For the spallation at/close to the interface of two ceramic layers in GZ/YSZ coatings, it is mainly caused by the following reasons: (1) there are more defects at the GZ/YSZ interface introduced in the sample preparation process; (2) the abrupt change of thermo-mechanical properties at the GZ/YSZ interface. This can be alleviated by adding a transition layer of 50wt% GZ+ 50wt% YSZ. As shown in three ceramic-layered TBCs, the ceramic interface was not the weakest place to initiate the cracks; (3) the interfacial stress resulted from the sintering effect of GZ. Since the thermal expansion coefficients of GZ and YSZ are very close, the spallation of GZ is not mainly from the thermal mismatch of the two ceramic materials. Because GZ has more globular pores and intersplat pores than YSZ layer, the sintering effect of GZ is more evident, which results in the volume and surface contraction of GZ. The shrinking surface introduces the in-plane tensile stress and causes cracks perpendicular to the surface, as shown in GZ/GZ50%/YSZ coating after thermal cycling at different temperature (Fig.4.7.6). The horizontal cracks in GZ layer are developed when the in-plane tensile stress accumulates to some extent. The coalescence of horizontal cracks combined with extension of vertical cracks result in the delamination and spallation of ceramic layer mostly from the YSZ layer.

One thing should be pointed out is that all of the coatings were tested in the air furnace except for the test with cooling in which the sample didn’t fail after 706 cycles, which means that there was less thermal gradient in the samples than that in a burner-rig test. The GZ ceramic layer could not effectively protest the bond coat from the high temperature. The designed working temperature of the bond coat in this study was below 950 ºC. So the severe oxidation of the bond coat was the most important reason for the short lives of all the coatings.

5. Conclusions:

5.1: For the evolution of hot corrosion resistance of YSZ, $Gd_2Zr_2O_7$, and $Gd_2Zr_2O_7$+YSZ composite thermal barrier coatings, the following conclusions can be drawn.

Under a typical gas turbine working temperature of 1050°C, the reactions between yttria (Y_2O_3) and V_2O_5 / $NaVO_3$ produce YVO_4, leaching Y_2O_3 from the YSZ and causing progressive tetragonal to monoclinic destabilization transformation. Based on hot corrosion chemical reactions formulas, the amount of corrosive salt charged in the tests was enough to react with the entire YSZ and $Gd_2Zr_2O_7$ layers (20 mg/cm^2 per cycle). After 20 hours (5 cycles) of hot corrosion test at 1050°C, the failure of the YSZ TBCs has initiated and propagated throughout the entire top coat, and led to the top coat delamination and spallation near the top coat–bond coat interface. The YSZ cross section shows severe macro-cracks and enhanced porosity due to the hot corrosion from the Na_2SO_4+V_2O_5 molten salts. For YSZ+$Gd_2Zr_2O_7$ coating, molten Na_2SO_4+V_2O_5 mixture reacts with $Gd_2Zr_2O_7$ to form $GdVO_4$ and monoclinic ZrO_2. The production of $GdVO_4$ predominately consumes V_2O_5 and thus postpones the formation of YVO_4 crystals and consequently less monoclinic ZrO_2 and less YVO_4 crystals are formed. On the surface of the YSZ+$Gd_2Zr_2O_7$ composite coating, YVO_4 crystals, are significantly smaller (about 20 μm in length) than the large rod shaped YVO_4 found in the conventional YSZ coatings (about 50 μm in length). The presence of fine-grained $Gd_2Zr_2O_7$ around YSZ particles also reduces the direct contact of conventional YSZ with molten salt, thus a better corrosion resistance. Molten Na_2SO_4+V_2O_5 mixture may also react with $Gd_2Zr_2O_7$ coating. However, unlike the YSZ case, where the molten salts attack the stabilizer Y_2O_3, molten Na_2SO_4+V_2O_5 mixture reacts with the bulk $Gd_2Zr_2O_7$ layer to form $GdVO_4$ and monoclinic ZrO_2. Under this accelerated hot corrosion test, bulk $Gd_2Zr_2O_7$ layer started to degrade after 36 hours of hot corrosion testing (9 cycles), which is much better than the YSZ case, which started to fail after 5 cycles. Also based on the results, $Gd_2Zr_2O_7$ layer provides a slightly better hot corrosion resistance than YSZ+$Gd_2Zr_2O_7$ coating. The chemical interactions, and the induced phase transformation, are the primary factors for degradation and spallation of the conventional YSZ and $Gd_2Zr_2O_7$ coatings. Based on the degradation rate, the corrosive layer thickness, and the general status of the coating after hot corrosion, $Gd_2Zr_2O_7$ containing coatings have a better hot corrosion resistance at a temperature of 1050°C than that of YSZ coatings.

5.2: For Phase stability and hot corrosion behavior of ZrO_2-Ta_2O_5 compounds, the following conclusions can be drawn.

The hot corrosion resistances of different compositions of YSZ, ZrO_2, and Ta_2O_5 samples to Na_2SO_4 + V_2O_5 mixture were studied, under a typical gas turbine component surface temperature of 1100˚C. The samples were selected to form both tetragonal and orthorhombic zirconium-tantalum oxides. Results show that orthorhombic zirconium-tantalum oxide is more stable, both thermally and chemically in Na_2SO_4+V_2O_5 media at 1100˚C, and shows a better hot corrosion resistance than the tetragonal phase. Thus orthorhombic zirconium-tantalum oxides offers good opportunities for developing novel TBCs with improved resistance to corrosion by sulfate/vanadate melts.

5.3: For thermal cycling, the following conclusions can be drawn.

$Gd_2Zr_2O_7$ is a potential candidate for TBCs applications. However, its reaction with the TGO layer makes it must be used in combination with an insulator layer, usually in the form of double or multiple ceramic-layered TBCs. In the present work, XRD results showed that the lattice constants of GZ structure in the mixture of 50wt% GZ + 50wt% YSZ powder decreased with the increase of hold duration at 1300 ºC, which indicated that there might be an order-disorder phase transformation due to the ion diffusion in the GZ/YSZ mixture. The reduction of relative intensities of YSZ to GZ in XRD indicated that YSZ tended to transform into GZ phase in the process of heat treatment, which would cause the volume change and the internal stress. This might be one of reasons for the interface failure in double-layered or functionally gradient TBC systems.

The thermal cycling behaviors of single ceramic-layered GZ, YSZ coatings, double ceramic-layered GZ/YSZ, GZ50%/YSZ coatings and three ceramic-layered GZ/GZ50%/YSZ coatings were investigated at different thermal conditions. Results showed that GZ based TBCs were mainly failed by delamination at the edge in YSZ layer close to the YSZ/TGO interface, bucking and spallation at/close to the interface of two ceramic layers. Edge and buckle-driven delamination were motivated by the compression in the TGO around interface imperfections caused by TGO growth and thermal expansion misfit between the ceramic layer and the bond coat upon cooling. The tensile stresses that arise around undulations and the associated energy release rate govern the crack nucleation, propagation and coalescence. The tensile stresses at the edge caused by the cool shock phenomenon during the cooling step were also contributed to the edge delamination. Thermal cycling amplified the energy release rates and accelerated TBCs failure through enlarging imperfections by a ratcheting mechanism.

The spallation at/close to the interface of two ceramic layers in GZ/YSZ coatings was mainly caused by defects at the GZ/YSZ interface introduced in the sample preparation process, the abrupt change of thermo-mechanical properties at the GZ/YSZ interface, and the interfacial stress resulted from the sintering effect of GZ. Sintering of GZ shrinked the ceramic layer, introduced the in-plane tensile stress and caused the vertical cracks, which usually initiated from the top layer due to the restriction of inner layer inside of TBCs during the thermal cycling.

5.4: For simulation, the following conclusions can be drawn.

The combination research of DFT based modeling, HPC MD simulation, and experiment validation study on novel TBC for gas turbine application was conducted. This integrated method as has been shown from other materials research can accelerate novel thermal barrier coating design and save tremendous expenses. For element component that includes *f* electrons, more accurate method such as quantum Monte-Carlo or self-consistent GW methods are needed to get more accurate inter-atomic interaction potentials and energy. The recent developed multicomponent alloys such as Hf-Mo-Nb-Ta-Ti-Zr etc. may serve as a better candidate for efficient bond coating for ultra high temperature applications. For other multicomponent metallic bond coating, extra metal dopants and/or diffusion barrier(s) such as Ta, Ti, and Al etc., may be needed and optimized to fit those high temperature and pressure requirements. The simulation and experiment both show that the $TaZr_{2.75}O_8$ with possible minor other dopants can have better corrosion resistance and stability than current YSZ top coatings etc.

Our simulation works on top coat $Gd_2Zr_2O_7$ study shows that doping Ti into both bond coat and top coat can enhance the bonding strength of the top/bond coat and improve the performance of the original top coat itself. The synchrotron XRD shear stress texture study is an effective technique to understand in-situ dislocation dynamics at nano-scale and boost new modeling and simulation research and thus assist novel high performance TBC design. More transition/rare earth metal elements may be needed to optimize the high temperature properties of the thermal barrier coatings. In addition, other different dopants such as rare earth oxide effects, grain boundary defects such as twin and other dislocations, high pressure and controllable particle size effects may be the key research topics in the near future.

Graphical Materials List

Published papers

(1). B. Zhang, M. C. Gao, Y. Zhang, S. Yang, and S. M. Guo, "*Senary refractory high-entropy alloy MoNbTaTiVW*", Materials Science and Technology, (2015).
(Web: http://dx.doi.org/10.1179/1743284715Y.0000000031)

(2). B. Chen, K. Lutker, J. Lei, J. Yuan, S. Yang, and H.K. Mao, "*Detecting grain rotation at nanoscale*", PNAS **111**, 3350 (2014).
(Web: http://www.pnas.org/content/111/9/3350)

(3). J. Lei, B. Chen, S. Guo, K. Wang, L. Tan, E. Khosravi, J. Yuan, S. V. Raju , and S. Yang, "*Structural and mechanical stability of dilute yttrium doped chromium*", Applied Physics Letters **102**, 021901 (2013).
(Web: http://apl.aip.org/resource/1/applab/v102/i2/p021901_s1)

(4). L. Tan and S. Yang, "*First principles calculation of Nb_2AlC/Nb interfaces*", JOM **65**, 326 (2013). (Web: http://link.springer.com/article/10.1007%2Fs11837-012-0548-1)

(5). B. Chen, S. V. Raju, J. Yuan, W. Kanitpanyacharon, J. Lei, S. Yang, H. R. Wenk, H. K. Mao, and Q. C. Williams, "*Texture of nanocrystalline nickel: probing the lower size limit of dislocation activity*", Science **338**, 1448 (2012).
(Web: http://www.sciencemag.org/content/338/6113/1448.short)

(6). M. H. Habibi, S. Yang, and S. Guo, "*Phase stability and hot corrosion behavior of ZrO_2-Ta_2O_5 compound in Na_2SO_4-V_2O_5 mixtures at elevated temperatures*", Ceramic International **40**, 4077 (2014).
(Web: http://www.sciencedirect.com/science/article/pii/S0272884213010201)

(7) M.H. Habibi, S.M. Guo, 2015, "*The Hot Corrosion Behavior of Plasma Sprayed Zirconia Coatings Stabilized with Yttria, Ceria, and Titania in Sodium Sulfate and Vanadium Oxide*", Materials and Corrosion, v 66, n 3, p 270-277, March 1, 2015 DOI: 10.1002/maco.201307331

(8) M.H. Habibi, S.M. Guo, 2014, "*Evolution of Hot Corrosion Behavior of YSZ-Ta_2O_5 Composites with Different YSZ/Ta_2O_5 Ratios*", International Journal of Applied Ceramic Technology, JAN 2014, pp1-9, DOI: 10.1111/ijac.12224

(9). M.H. Habibi, Li Wang, Jiandong Liang, and S.M. Guo, 2013, "*An Investigation on Hot Corrosion Behavior of YSZ-Ta_2O_5 in $Na_2SO_4+V_2O_5$ Salt at 1100˚C*", Corrosion Science, V75, No.10. pp 409-414, http://dx.doi.org/10.1016/j.corsci.2013.06.025

(10). M.H. Habibi, Li Wang, S.M. Guo, 2012, "*Evolution of hot corrosion resistance of YSZ, $Gd_2Zr_2O^7$, and $Gd_2Zr_2O_7$+YSZ composite thermal barrier coatings in $Na_2SO_4+V_2O_5$ at 1050°C*", Journal of the European Ceramic Society, 10.1016/j.jeurceramsoc.2012.01.006

LIST OF ACRONYMS AND ABBREVIATIONS

DFT	density functional theory
DSC	differential scanning calorimetry
FWHM	full width at half maximum
HPC	high performance computing
MC	Monte Carlo method
MD	molecular dynamics
MedeA	Materials Design software
SEM	scanning electron microscopy
TBC	thermal barrier coating
TGA	thermogravimetric analysis
XRD	x-ray powder diffraction
YSZ	yttria stabilized zirconia